Deformation of Aluminum Investigated by Digital Image Correlation: Evidence of Simultaneous Crystal Slip and Grain Boundary Sliding

A. Dimanov, A. El Sabbagh, J. Raphanel, M. Bornert, Thien-Nga LE, S. Hallais, A. Tanguy

Deformation of aluminum investigated by digital image correlation: evidence of simultaneous crystal slip and grain boundary sliding

A.Dimanov[a,§], A. El Sabbagh[a], J. Raphanel[a], M. Bornert[b], L. Thien-Nga[a], S. Hallais[a], A. Tanguy[a]

[a]*Laboratoire de Mécanique des Solides, CNRS UMR 7649, École Polytechnique, F- 91128, Palaiseau Cedex, France.*

[b]*Laboratoire Navier, CNRS UMR 8205, École des Ponts, Univ. G. Eiffel, F-77420 Champs sur Marne, France*

[§] Correspondence should be sent to: thien-nga.le@polytechnique.edu

Code de champ modifié

All Figures should be printed in color, except for # 3, 13, 14, 15, 17, 18

Abstract

We investigate the multiscale micromechanical behavior of nearly pure polycrystalline aluminum exhibiting randomly oriented coarse grains (ca. 300 μm in size) between room temperature and 400°C. We present results from *in situ* mechanical testing obtained through scanning electron microscopy and full-field strain measurements by digital image correlation (DIC) during uniaxial compression, with controlled displacement rate. Direct observation of the process of developing strain heterogeneities allows for identification of the active mechanisms, characterization of their interactions and quantification of their respective contributions to the overall strain. The full-field strain measurements were carried out, from the sample scale, to the scales of the aggregate of grains, and finally the single grain. DIC analysis was performed thanks to specific surface marking patterns obtained by electron microlithography appropriate for the different scales of interest. The strain localization patterns showed dominant crystal plasticity. Except at room temperature, we always observed simultaneous and continuous activity of grain boundary sliding, whose relative contribution increased with temperature. We suggest that for coarse-grained microstructures grain boundary sliding acts as a complementary mechanism for the accommodation of local plastic incompatibilities inherent to the anisotropy of crystal plasticity.

Keywords: 1-Methods of investigation: electron microscopy, micromechanics, stress/strain measurements, **2-Material and constituting phases:** aluminum alloys, **4-Investigated phenomena:** grains and interfaces, plasticity and temperature, **Other:** Digital Image Correlation

1.Introduction

Understanding and modeling viscoplastic deformation of polycrystalline materials is essential for the control of hot-forming processes and, more generally, for an estimate of the durability of functional metallic structures submitted to extreme thermomechanical constraints. During such a process a zoology of microphysical mechanisms may come into play, which involve temperature, stress and strain rate conditions, as well as the microstructure of the material. The active mechanisms to which we shall refer may exist in metallic or iono-covalent polycrystals of any grain size, in this particular study we shall focus on the model metal aluminium with rather large grain size. This work will among other mechanisms point out the rôle of grain boundary sliding and the necessity to go beyond the picture conveyed by the usual "deformation mechanisms maps". Realistic modeling of polycrystalline viscoplasticity is therefore subordinated to detailed understanding of the interactions between these different mechanisms. Most of the time, however, the microstructural observations enabling to identify the possible active mechanisms through their specific microstructural signatures are performed *post mortem*. Consequently, the chronology of activation and the interactions between the different mechanisms remain unclear. It is necessary

therefore to identify and quantify these processes by *in situ* monitoring at the appropriate scales. Full-field measurements based on the analysis by digital image correlation (DIC) of sequences of images recorded by scanning electron microscopy (SEM) during *in situ* mechanical tests is the most suited experimental technique for the micromechanical characterization of strain localization down to the grain scale [1]. This approach enables, for instance, to identify the active mechanisms, to characterize their interactions and to calculate their respective contributions all along the loading process [2], [3], [4], [5], [6].

We developed our own setup for SEM *in situ* thermomechanical testing, specifically devoted to DIC-based full field measurements. The device enables to perform simple compression/tension and bending tests at both room and high temperatures. While similar facilities are commercially available [7], we chose to build our own devices for possible further developments to reduce costs. The principle of full-field measurements by DIC relies on the presence of local contrasts within the material. Each material point may be defined uniquely on the basis of a specific signature in terms of the surrounding local gray levels. These signatures are used as kinematic markers in order to determine the displacement fields during the mechanical deformation. The contrasts can be natural if the material is poly-phase [8]. For single-phase polycrystalline materials observed in SEM the contrasts are provided artificially [9], [10], [2]. In the present work we studied nearly pure aluminum, containing only 0.1 wt% Mn [11]. The initial material was extracted from the central part of rolled aluminum plates. Heat processing at 500°C resulted in a balanced and nearly non-textured microstructure, with coarse grain sizes of several hundreds of micrometers. Electron microlithography [9] was used in order to produce regular platinum fiducial micro-grids onto the sample surface.

Our deformation rig allows for observation over the entire specimen surface. Contactless thermal monitoring and control is ensured by *in situ* infrared pyrometry. Parallelepiped samples 4x4x6 mm^3 were axially shortened stepwise up to 5 - 10 % at temperatures ranging between room conditions and 300°C. High quality SEM images with several magnifications were obtained at each deformation step and further analyzed by DIC (using in-house CMV software), in order to obtain in-plane displacement fields and calculate in-plane strain fields [4], [5], [8], [9], [12], [13], [14]. The experimental details and analytical procedures are given in the following sections.

Mis en forme : Couleur de police : Rouge
Mis en forme : Couleur de police : Rouge
Mis en forme : Couleur de police : Rouge
Mis en forme : Couleur de police : Rouge
Mis en forme : Couleur de police : Rouge
Mis en forme : Couleur de police : Rouge
Mis en forme : Couleur de police : Rouge
Mis en forme : Couleur de police : Rouge

2. Experimental and analytical procedures

2.1. In-situ SEM thermomechanical testing stage

The experimental setup is fitted to the original sample holder stage of a QUANTA 650 FEG-ESEM. The microscope is equipped for electron back scatter diffraction (EBSD), with a HKL Nordlys II S camera operated with Aztek 3.1 and Channel 5 data post-processing software. The rig frame is machined out of stainless steel and is U-shaped in order to provide maximum accessibility to the loading column and the sample (Fig. 1). Compression

is driven by a conventional DC-motor Mattke 3557-K024C (nominal rotation speed and torque of 3000 rpm and 0.040 Nm, respectively). A gear train reduces the rotation speed while increasing the torque. Rotation transforms into translation thanks to a screw nut system and the crosshead glides on linear ball bearings along two stainless steel shafts. The mobile crosshead is equipped with a linear displacement sensor (optical rule type from Solartron), which is attached to the frame and measures the displacements for a homemade controller which allows loading rates as low as 0.1 μms^{-1}. The loading capacity is 5 kN. The exerted force is measured by an Ametek load cell inserted within the assembly of the loading column and the frame (Fig. 1). The compression stroke ranges within 12 mm.

Heating parts and temperature monitoring: The testing system is designed to offer the entire sample surface free for observation. For that purpose, two tubular furnaces are fitted to the pistons and the sample is heated by sole conduction. The two assemblies of pistons and their tubular resistors are thermally insulated by cylindrical ceramic shields. We used SiC pistons which are connected to the rig frame with metallic wires, hence avoiding electrical charging. Precise temperature monitoring is usually obtained by attaching or directly welding a thermocouple on the sample. In order to avoid any risk of local alloying, or loss of contact during sample deformation, we developed contactless measurements obtained with an infrared pyrometer fitted within the SEM chamber and targeting the sample laterally (Fig. 1). The tests last several hours, therefore a cooling circuit is fitted to protect the electronic circuits, load cell and actuator. The cooling circuit is composed of flexible silicone tubes connecting two stainless steel parts and a chiller centrifugal pump providing continuous cooling flow, the temperature being adjusted according to the experimental set point. One of the water-cooled steel elements is inserted in-between the insulated heating element and the load-cell, which is attached to the frame. The other one is placed between the second insulated heating element and the crosshead of the loading column (Fig. 1). All these elements are precisely aligned in order to avoid stress concentrations in the ceramic parts. The temperature of the load-cell is monitored by a Pt100 sensor.

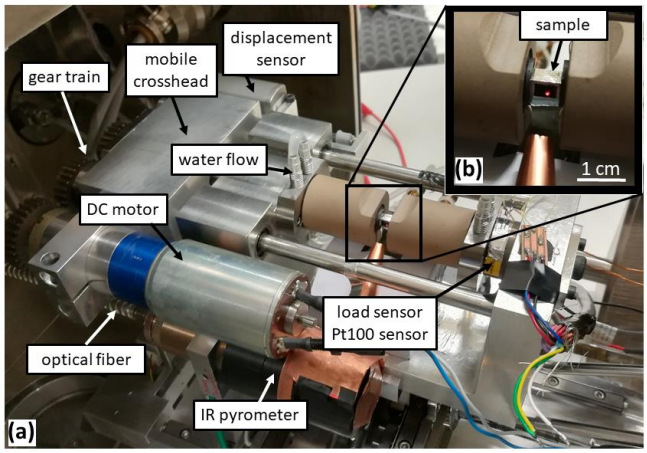

Figure 1: (a): SEM chamber with the in-situ testing setup, composed of the axial compression deformation machine, the tubular heating elements surrounding SiC pistons (shielded by pyrophilite ceramics) and the IR-pyrometer. A liquid cooling circuit protects the mobile crosshead (on the left hand) and the gear train, and the load sensor (on the right hand). (b): focus on the sample targeted by the infrared pyrometer. The laser centering spot is visible on the 6 mm-long aluminum sample, whose lateral surface is painted in black. Parasite IR radiations are avoided by covering the pyrometer with copper foil and collecting exclusively the radiations emitted by the sample with a copper funnel.

The heat is generated by two heating resistors with bi-directional wiring of 1.1 Ω each (40 W). The bi-directional wiring prevents the development of magnetic fields which could disturb the electron beam. The resistors consist of platinum wires (0.3 mm in diameter) embedded in multi-layered ceramic insulation. PID controlled current is provided by a switch-mode DC power supply (maximum output: 20V/20A). The heating elements are placed around two sintered SiC pistons, chosen for their appropriate mechanical strength and thermal conductivity. Symmetrical heating of the sample is obtained by conduction through the pistons, which have precisely flat and mirror polished end surfaces to ensure good contact and heat transfer to the sample, but also to reduce interfacial frictions. Insulating shields made of annealed pyrophyllite (aluminosilicate ceramic) limit radiative loss. The starting pyrophyllite material is soft and easy to machine in its naturally hydrated form. After machining, the pyrophyllite shield pieces are dehydrated by annealing at 1300°C for about 4 hours, reaching a compressive strength of about 80 MPa. The complete experimental setup is shown in Fig. 1. The details on the *in situ* SEM pyrometer are given in the following section.

2.2. Contactless temperature measurement and monitoring

The development of this system was motivated by the geometrical constraints of the heating apparatus, which excludes the introduction of a thermocouple close enough to the sample which would still leave the whole

area observable. On the other hand, the aluminum sample and the experimental temperature range do not allow for easy welding or sticking of a thermocouple on the sample back side without risk of losing contact during loading. Therefore, we adapted an infrared pyrometer Lumasens IGA 320/23-LO for contactless measurements of sample temperature inside the SEM chamber. The emitted infrared radiation is transmitted by a mirror to the optical device of the pyrometer located in the SEM chamber, which is connected via an optical fiber to the detector and electronic circuit located outside the SEM (Fig. 1). The focal distance can vary between 8.8 cm and 11 cm, which allows for an accurate focus on the surface of the sample with a spot size of 0.8 mm. The considered wavelengths range between 2 and 2.6 mm. Temperature measurement ranges between 100°C and 700°C, with an overall estimated accuracy within 3°C. A mirror deflects the infrared radiations from the sample to the pyrometer optics, which are clamped aside the rig (Fig. 1). The optical axis is aligned at 60° to the normal of the sample's side. The deflecting mirror is protected by a copper shield, in order to avoid parasite emissions from the chamber, the setup and more specifically from the heating elements. The only measured infrared signal is collected by a copper funnel operating as a waveguide from the sample side to the deflecting mirror (Fig. 1).

According to the Stefan-Boltzmann law the irradiance is proportional to the fourth power of the temperature. Therefore, the reading of the pyrometer matches the intensity of infrared radiations within the considered wavelength range emitted by the sample. The emissivity coefficient ε of the sample represents the ratio of its real radiative emission and that of the theoretical black body. Together with the Stefan-Boltzmann constant it represents the proportionality between radiation intensity and temperature. The higher is ε, the better is the measurement. Metals are called selective bodies, because their emissivity coefficients are usually low, but also temperature and wavelength dependent. In the present case ε may be assumed constant over the limited wavelength range. Yet for aluminium $\varepsilon = 0,3$, which is very low. We improved the emissivity coefficient up to $\varepsilon = 0,64$ by spraying thermo-resistant black paint onto the sample surface targeted by the pyrometer optical line.

The pyrometer is initially calibrated for atmospheric conditions, which means 10^5 Pa total air pressure, in the presence of water vapor, which is very absorbent in the wavelength range of interest. Therefore, we specifically calibrated the measurements for the high vacuum of the SEM chamber (10^{-3} Pa). We actually made corrections to the emissivity coefficient for each experimental temperature. For that purpose, we prepared a replica aluminum sample, of dimensions identical to those of the samples used for mechanical testing. K-type thermocouple was inserted within a borehole of 0.5 mm drilled in the center of the sample. The corresponding temperature was used as reference for the pyrometer read-out, while adjusting the emissivity coefficient parameter.

2.3. Material and sample preparation

In line with previous studies [11], ~~[46]~~, [15], the initial material is nearly pure aluminum, with only 0.1 wt. %. of manganese. This alloying element reduces the mobility of grain boundaries by solute drag effect [11]. Thermal

Mis en forme : Couleur de police : Rouge

Mis en forme : Couleur de police : Rouge, Barré

Mis en forme : Couleur de police : Rouge

Mis en forme : Couleur de police : Rouge

stability of the microstructure is important for *in situ* strain measurements, because migrating grain boundaries may i) hide the contribution of pure grain boundary sliding, ii) limit the cumulative strain analysis. The material is a single phase polycrystal with a face centered cubic structure. These characteristics render possible a precise analysis of the micro-mechanisms that take place in the course of plastic deformation ([16], [17]). The material has low melting point (667°C) and yield strength (a few MPa), and hence the setup permits exploration of a wide range of experimental conditions and activation of different potential mechanisms ~~[45],~~ [16], [17], [18], [19], ~~[15],~~ [20], [21].

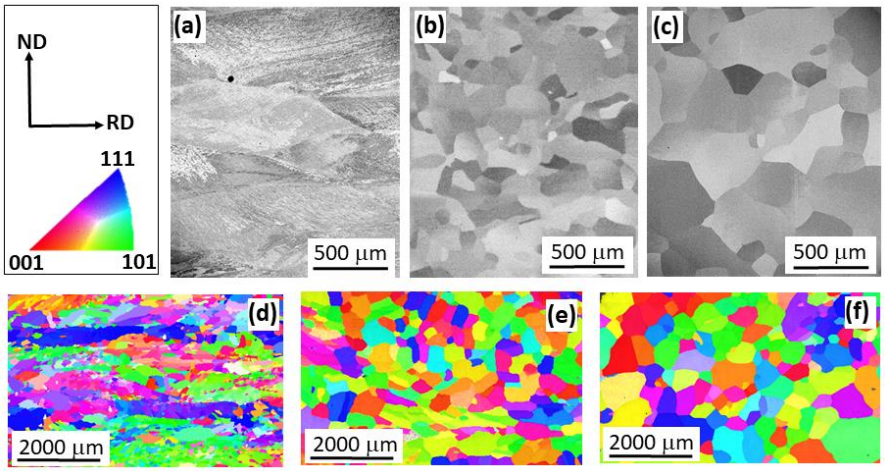

Figure 2: Material microstructures. (a): Backscattering SEM micrograph from starting cold-rolled material. Normal Direction (ND) and Rolling Direction (RD) are indicated on the left hand. (b) and (c): Backscattering SEM micrographs from materials annealed at 500°C for 5 and 30 minutes, respectively. (d), (e) and (f): Inverse pole Figure (IPF) maps with respect to the IPF color reference and transverse direction (TD), orthogonal to the RD and ND directions as defined on the left-hand of (a). (d): IPF map from cold-rolled material. (e) and (f): IPF map from materials annealed at 500°C for 5 and 30 minutes, respectively.

The starting material Al-0.1Mn (Alcan CRV, ingot series 3442 C) was kindly supplied by R. Quey (Laboratoire Georges Friedel, Ecole des Mines de Saint-Etienne, [15]) in the form of slabs of 100x60x20 mm, cold rolled up to 0.5 total strain.The samples are cut out from the central part of cold rolled slabs in order to limit microstructural gradients due to boundary effects. Samples are parallelepiped shaped (4x4x6 mm^3), with the rolling direction parallel to their longest dimension, which is also meant to be the compression axis. Annealing at 500°C for 5 minutes strongly reduces the initial rolling texture, and results in a fairly homogeneous and equant recrystallized microstructure. Further annealing for 30 minutes achieves equilibrated coarse-grained microstructure

Mis en forme : Couleur de police : Rouge

Mis en forme : Couleur de police : Rouge, Barré

Mis en forme : Couleur de police : Rouge

Mis en forme : Couleur de police : Rouge, Barré

Mis en forme : Couleur de police : Rouge

Mis en forme : Couleur de police : Rouge

(Fig. 2). In spite of the Mn solute, at such high temperature mobility of grain boundaries is fast enough to obtain a coarse-grained and equant microstructure (Fig. 2). The mean grain size obtained by the intercept method is of 300 µm and shows a mean aspect ratio of 1.2. The grain size distribution is unimodal, but spread (100 - 1000 µm), ~~[221]~~. The annealed samples are first mechanically polished with SiC grinding papers down to 4000 grade (5 µm particle) and secondly with diamond paste down to 3 µm. Mirror quality finish is obtained by electro-polishing with a commercial STRUERS A2 electrolyte solution. The procedure removes the cold worked zone, ensuring a good crystalline surface state adequate for EBSD analysis (Fig. 2), but may result in some etch pits. Samples are selected to present homogeneous and non-textured microstructure, such as in Fig. 2c and Fig. 2f.

Mis en forme : Couleur de police : Rouge, Barré

2.4. Digital image correlation

Digital image correlation (DIC) is a computational technique, aiming at the characterization of the mechanical transformation connecting an image from an actual (deformed) state to an image from a previous (reference) state. In our case we applied 2D DIC, which implies solely the characterization of in-plane displacement and strain. The DIC method relies on the existence of local contrasts, i.e. fluctuating grey levels, which can be assigned to the surficial material points as characteristic signatures. In practice the procedure aims to determine the surficial displacement field of material points that are discretely distributed following a periodic pattern like a grid. These measurement points are centered within restricted domains, called correlation windows, where grey scale level is considered as the discriminative signature of the measurement point. The in-plane components of the displacement field corresponding to the mechanical transformation between the reference and the actual states is obtained by the minimization of the so-called correlation coefficient, defined on the basis of the grey levels of the pixels in the correlation windows in the reference and actual images. The corresponding in-plane deformation gradient components are computed following different local integration schemes, based on a contour integral defined by a chosen number (usually from 4 to 8) of nearest neighboring measurement points. The computation of the in-plane strain components depends on some additional hypotheses (namely limited local out of plane rotations). The accuracy of strain computation increases with the number of considered neighboring points (large contour integral). Conversely, the spatial resolution of the computed strain field decreases due to the increasing local gage length. For details see [1], [2], [4], [8] ~~[5]~~.

Mis en forme : Couleur de police : Rouge

Mis en forme : Couleur de police : Rouge

Mis en forme : Couleur de police : Rouge, Barré

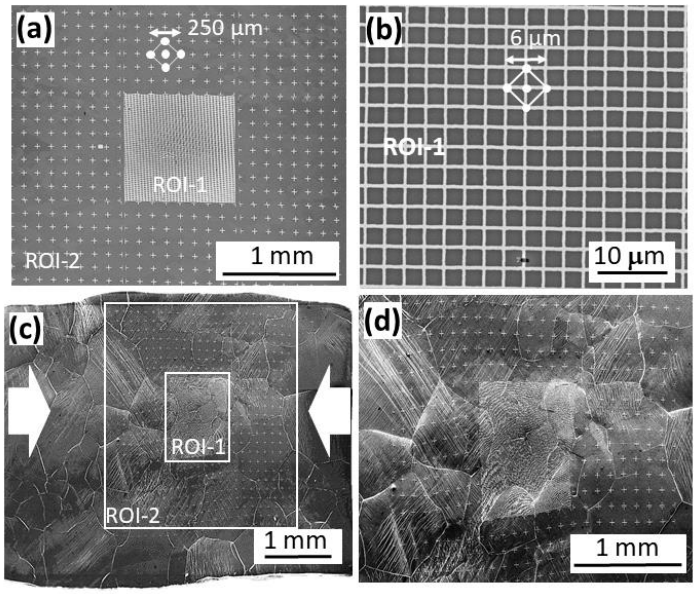

Figure 3: SEM micrographs showing the two-scale typical patterns of platinum deposit obtained by electron-microlithography (before and after deformation). a: Crosses are distant one another by 125 µm (gage length 250 µm) and cover the ROI-2 of 3x3 mm2. ROI-1 covers 1x1 mm2 in the middle of ROI-2. b: Detail of the central grid pattern of ROI-1, with 3 mm pitch. The pattern is used to calculate the local strain fields at the measurement points corresponding to the grid intersections. The strain computation contour is based on the nearest 4 neighbours, as schematically indicated in the middle of the image, hence resulting in a local gage length of 6 µm. c: Low magnification view of a whole specimen deformed at 300°C up to 5% horizontal overall shortening. d: Central part of the specimen in (c). The cross-marked ROI-2 enables to compute the strain field with low resolution, (but high accuracy) over a large area and to quantify the average sample shortening. The central grid-marked ROI-1 allows to compute highly spatially-resolved kinematic fields, in order to identify and quantify the deformation mechanisms.

In our case, the local contrasts are provided artificially. The layout of randomly dispersed markers is often applied for DIC analysis [2], [22], [23], [24], [25], [26], [27], [28], [29], [30]. We applied however SEM micro-lithography for the laying of thin ductile metallic regular patterns onto the observed surfaces of the samples, which is also a very common technique [9], [31], [32], [33], [34], [35]. The main reason is that this technique allows to precisely control the size of the marking pattern, and therefore to adapt the local strain gage for DIC analysis with respect to differently-sized observation areas, corresponding to different analytical targets. On the one hand, this approach allowed us to compute the strain with very high spatial resolution over a restricted part of the sample surface corresponding to a group of grains, in order to investigate at the grain-scale the strain heterogeneities developing in relation to the local interactions between neighbouring grains. On the other hand, we could perform

less resolved but fast and accurate computation of the strain over the larger part of the sample surface, in order to obtain accurate measurements of the overall strain components for a representative area of the polycrystalline material. We will not elaborate on the details of the technique, which is well documented in the literature [9], [31], [32], [33], [34], [35]. But we must specify that the choice of the metal to be deposited depends on its stability with respect to the substrate and the experimental temperatures. The grid marking patterns are usually made of gold. However, gold alloys with aluminum and thin gold films are easily dewetted at temperatures of 300°C and above ([2]). Therefore, instead of gold our choice went to platinum.

For more details on SEM *in situ* micromechanical testing and DIC analysis the reader is referred to more than two decades of developments and practice ~~[4], [5],~~ [1], [4], [10], [36], [37]. In our case, following the procedures applied in ~~[2] and [9]~~ [9] and [13] the measurement points of the computational array can be centered at the intersections of the surficial platinum grid, as shown schematically in Fig. 3b. In this present case, the chosen configuration of 4 neighbors defines a lozenge-shaped integration contour. The resulting local gage length of 6 µm determines the spatial resolution of the in-plane computed strain field. The Pt surficial grid pitch may be adjusted depending on the resolution wanted for the computed in-plane strain field. We have selected two regions of interest (ROI). ROI-1 represents 1 mm^2 centered within the sample observation surface (6x4mm^2). ROI-2 represents 3x3 mm^2 surrounding ROI-1. ROI-2 excludes the sample borders that may be affected by end effects and fretting, but remains large enough to be representative of the strain experienced by the specimen as a whole. The mean strain components are computed over the ROI-2 with a large gage length (ca. 250 µm), masking fine scale heterogeneities, but ensuring computational accuracy and speed. Nearly real-time DIC can be performed at the mesoscopic scale over ROI-2, providing a better monitoring of the deformation process than relying on the displacement sensor of the crosshead whose measurement is affected by the compliance of the mini-rig. The pattern of the deposited platinum covering the ROI-2 represents a regular grid of crosses with a pitch of 125 µm (Fig. 3), that remains substantially lower than the mean grain size (ca 300 µm). ROI-1 is selected with respect to the homogeneity of the microstructure and the absence of remaining texture. The pattern of the deposited platinum covering the ROI-1 represents either a continuous regular grid, or a grid of irregular crosses (Fig. 3 and 4). This domain is meant for detailed investigation of strain heterogeneities and active mechanisms at the scales of the individual grain and the aggregate. The grid pitch is therefore reduced down to 3 µm (Fig. 3), allowing for computing with fine gage lengths (ca. 6 µm) and providing highly spatially-resolved strain fields. The grid lines are 600 nm wide, which represents a few pixels in width for the micrographs with resolution of 4096x3775 pixels.

Observed at low magnification, like in Fig. 3a, the fine scales grids of ROI-1 may exhibit a Moiré effect, due to the combination of subsampling (e-beam spot size smaller than pixel size) and slight shift between the marking grid and the scanning direction. The Moiré effect can be reduced with the use of a Gaussian filter during post-processing. The grid of measurement points devoted to DIC is adapted to the different marking patterns for

Mis en forme : Couleur de police : Rouge, Barré
Mis en forme : Couleur de police : Rouge
Mis en forme : Couleur de police : Rouge, Barré
Mis en forme : Couleur de police : Rouge
Mis en forme : Non Barré
Mis en forme : Non Barré

ROI-1 and ROI-2. For both the measurement points are located at the intersections of the grid and at the crosses, spaced by 12 and 171 pixels, respectively. For ROI-1, the correlation windows are 12x12 pixels, and hence the whole area is covered without overlapping of neighboring windows, which prevents smoothing of strain heterogeneities. The subpixel correlation is performed with a bilinear interpolation ~~[5]~~, ~~[4]~~, [12].

Mis en forme : Couleur de police : Rouge, Barré

Mis en forme : Non Barré

2.5. Strain computation

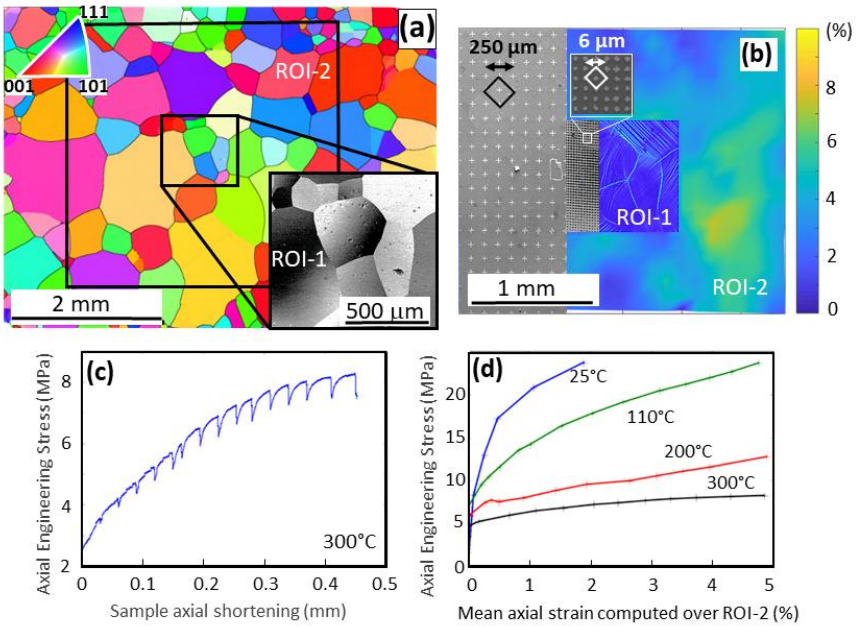

Figure 4: Schematic representation of the testing protocol. (a): IPF-x of a selected specimen, with the defined ROI-2 and ROI-1, and an inserted BSE image of ROI-1 in the right-hand lower corner. (b): Montage micrograph, showing i) on the left-hand the patterns of the two-scales surface marking, corresponding to ROI-2 and ROI-1 shown (a), ii) on the right-hand the respective computed equivalent strain maps, after ca. 3 % axial shortening at 200°C. The color scale is given in percent. The ROI-2 and ROI-1 strain maps have respectively low and high spatial resolutions, owing to their respectively large (250 µm) and small (6 µm) gage lengths. (c): Engineering stress-strain loading curve based on the data recorded by the load cell and the Solartron displacement sensor attached to the mobile crosshead. (d): Engineering stress-strain loading curves for samples compressed at 25°C, 110°C, 200°C and 300°C based on the data recorded by the load cell and the mean equivalent strain computed over ROI-2.

The DIC procedure delivers the displacement field of the measurement points, which allows strain computation. The integration contour we used to compute the local strain at each point is defined by the 4 nearest neighboring points (integration scheme 2, as defined in [2]). We recall that the grid of points has a pitch of 3 µm,

therefore the local gage length is of 6 μm (Fig. 3b). The DIC provides only the in-plane displacement components and thus we can only compute the corresponding components of the in-plane deformation gradient **F**: F_{11}, F_{22}, F_{12}, F_{21}. In order to compute the strain tensor some assumptions are necessary in the framework of small strains. First, the normal to the observation plane is considered to be a principal axis of deformation and no out-of-plane rotations are considered, which implies $F_{13} = F_{31} = 0$. The last hypothesis assumes axisymmetric conditions (transverse isotropy), which allows to estimate the out-of-plane ~~strain~~ eigenstrain.

Mis en forme : Couleur de police : Rouge, Barré

Two examples of strain computation at the scales of ROI-1 and ROI-2 are shown in Fig. 4. Their respective local strain gages are of 6 μm and 250 μm, hence the corresponding spatial resolutions. The relevant test was performed at 200°C, until axial shortening of about 2.5 %. The mean axial strain component is computed in real time during the test over the whole ROI-2 domain. The strain maps presented in Fig. 4 and in subsequent work show a scalar representation of the local plastic deformation. We use the second invariant of the deviatoric part of the in-plane strain tensor, which is the 2D analog to the "von Mises equivalent strain". With the above mentioned assumptions it may be written as $\varepsilon_{eq} = 2|\ \varepsilon_1 - \varepsilon_2|/3$, where ε_1 and ε_2 are the in-plane principal strain components.

2.6. In situ SEM testing protocol

A strict testing protocol was developed to ensure the reproducibility of the results. At first, the cooling circuit is stabilized at the cooling temperature corresponding to the testing high temperature, as established during the calibration procedures. Secondly, the load cell is preloaded at 100 N, the sample is inserted in between the SiC pistons, where it is held with an additional preload of 10 N. Correct sample positioning requires the observation surface and the painted lateral side to be perpendicular to the SEM column and to the pyrometer optical line, respectively. The pyrometer alignment is tuned by focusing its in-built LED onto the painted sample face. When vacuum reaches 10^{-3} Pa, the sample emissivity parameter is set to the value corresponding to the desired temperature (according to our calibration, see section 2.2) and the heaters are powered. During the heating and thermal expansion phase, the crosshead position is adjusted to maintain the pre-loading of the sample around 10 N. Equilibrium temperature is reached within less than an hour. The electron beam is set at 15 kV.

The initial state micrographs are the references for the correlation procedures. The reference state is also used to estimate the systematic errors, through the analysis of a known transformation, introduced by small variations of magnification and small translations. The deformation is done stepwise, by increments of nearly 0.5 % axial strain, at controlled crosshead displacement rate of 0.1 μms^{-1} corresponding to a strain rate of about 10^{-5} s^{-1}. The axial crosshead displacement is controlled by the displacement sensor, whilst the total average axial strain is monitored by a quick DIC computation, performed over the 3 mm - wide area (ROI-2) marked by large crosses (Fig. 3 and 4). Higher magnification micrographs are further collected over the central 1mm-wide ROI-1 area, marked by fine grids or crosses, in order to perform computations later on highly resolved full strain fields (Fig. 3

and 4). It is noteworthy that in Fig. 4c the loading curve is based on the axial displacements measured by the Solartron displacement sensor. Therefore, the mechanical behavior includes the compliance of the machine and the initial alignment of the whole loading column (crosshead, SiC pistons and sample). In Fig. 4d the loading curves are based on the mean axial strain computed by DIC over ROI-2, representing therefore only the behavior of the material. The sample is not unloaded after each deformation step, and thus, we can see on the loading curve in Fig. 4c the relaxations of the material corresponding to the duration of image acquisition.

2.7. Focused ion beam and transmission electron microscopy

After the mechanical testing, we used a FIB Helios-660 focused ion beam (in MSSMAT, Ecole Centrale Supelec) to mill small volumes of about 100 μm^3 around specific grain boundaries of interest. The excavation allows to reveal the geometry of the grain boundary at depth, and in particular its inclination. Secondly, we excavated cross section lamellae of ~ 20 µm long, ~ 10 µm large and ~ 2 µm thick across the chosen grain boundaries, in order to investigate the *post mortem* microstructures by transmission electron microscopy (TEM). Platinum films were deposited onto the surficial top edges of the lamellae, in order to protect the traces of the grain boundaries during ion milling. The machined lamellae were further thinned with a Gatan PIPS II and were observed with the Titan-Femis TEM operating at 300 kV (CIMEX platform, Ecole Polytechnique).

3. Results and discussion

Secondary electrons (SE) SEM micrographs and DIC-computed equivalent strain maps enable to detect strain localization and to identify the corresponding deformation mechanisms, such as crystal slip in individual grains. The SE micrographs may exhibit surface slip lines (or groups of slip lines forming slip bands) characterized by step-like topography, resulting from the out-of-plane crystal slip components. Conversely, the DIC-computed strain maps evidence the in-plane slip components of active slip systems. When both out-of-plane and in-plane slip components are present, SE and DIC observations reveal the same slip bands. In extreme cases, when the out-of-plane component of a slip system is negligible, the slip bands are evidenced solely by the DIC analysis. On the one hand, the DIC analysis of the ROI-1 areas allow to characterize and to precisely quantify strain localization phenomena at the microstructure and grain-scales. On the other hand, the DIC analysis of the ROI-2 areas allow to compute precisely the average axial strain for the central part of the specimen. The latter computed data and the macroscopic engineering stress (considering applied force and initial sample cross section) are used to plot the characteristic loading curves of strength versus axial strain shown in Fig. 4d. The advantages of such measurements with respect to the usual macroscopic records of strain by displacement sensors are to exclude machine-related effects (positioning of the loading column and frame compliance), but also to limit the sample-scale strain

heterogeneities related to piston fretting effects. The loading curves in Fig. 4d correspond to room temperature and three high temperatures: 110°C, 200°C and 300°C, representing respectively homologous temperatures of 0.4, 0.5 and 0.6. Yield strength and strain hardening rates decrease with increasing temperature. This behavior is typical for thermally activated dislocation recovery processes, among which dynamic recrystallization, which is highly dependent on strain rate and temperature [20]. The different aspects concerned with the operational deformation mechanisms will be addressed in more detail in the next sections on the basis of the obtained strain maps.

3.1. Influence of temperature on localization

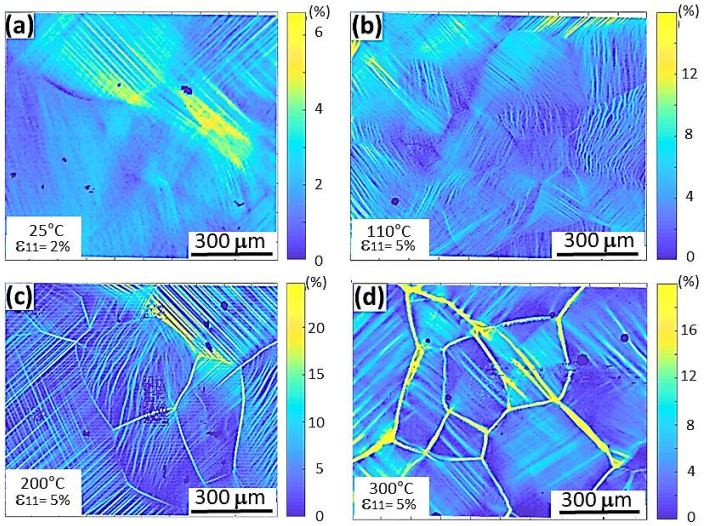

Figure 5: Typical equivalent strain maps computed over ROI-1. (a) Ambient temperature and 2% axial strain. (b) to (d) Respectively at 110°C, 200°C and 300°C and ca. 5% axial strain. Crystal plasticity is clearly evidenced by the presence of slip bands within individual grains, which are clearly identified by their respective localization patterns. Grain boundaries exhibit strong localization at 200°C and very strong localization at 300°C. Note that the strain maps are not at the same color scale. Scales are adapted to each case in order to highlight the intensities of localization features.

Fig. 5 summarizes the results of uniaxial compression tests performed at 25°C, 110°C, 200°C and 300°C. Fig. 5a to 5d present the equivalent strain maps computed by DIC over the central 1 mm-wide area (ROI-1) for the final deformation step, cumulating axial strains of ca. 2 % for room temperature and ca. 5 % for higher temperatures. Note that the color scale, given in strain %, is not the same for all the tests. Results from samples deformed at 400°C are not shown and will be briefly discussed later. All the strain maps present similarities, such as intra-granular or inter-granular localization features. For instance, intra-granular localization patterns represent discrete crystal slip

bands. Temperature-related differences of strain localization patterns are also evidenced. In general, it is observed that increasing temperature results in lower spatial density of slip bands, but in higher slip intensity. At moderate and intermediate temperatures (110°C and 200°C, respectively) we can see some similarities and some differences. At first, it is worthy to note that in both cases slip bands are essentially sharp. At moderate temperature (110°C) the spatial density of slip bands is high, but their strain intensity is low, and very little strain localizes at a few grain boundaries (Fig. 6d). At intermediate temperature (200°C) strain intensity of individual slip bands increases, whilst their spatial density decreases. Strong localization appears along most grain boundaries (Fig. 6e). At moderate temperature many grains present both wavy and straight slip band morphology. At intermediate temperature only few grains present wavy slip band morphology.

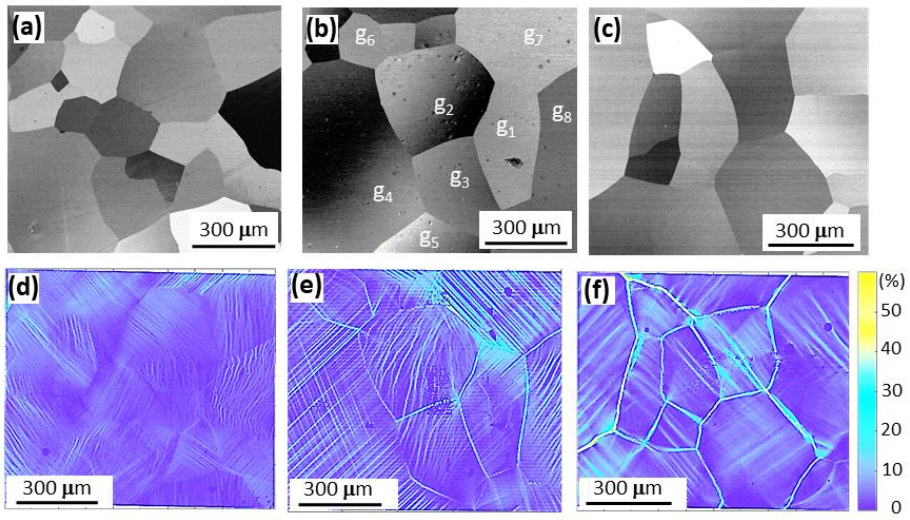

Figure 6: Microstructures and corresponding equivalent strain maps. (a), (b) and (c): BSE micrographs of ROI-1 areas. In (b) grains are individually labeled for further discussion. (d), (e) and (f): Equivalent strain maps respectively corresponding to (a), (b) and (c) microstructures. The strain maps correspond to these shown in Fig. 5, but presented with the same color scale.

At high temperature (300°C, Fig. 6f) slip bands present mostly straight, but very diffuse character. They broaden considerably, but lose their sharpness. These morphological features may be related to recovery processes which are increasingly active with temperature. Conversely, high temperature may induce activation and interplay of multiple slip systems, allowing to homogenize the spatial strain distribution. Strain localization at grain boundaries is also strongly enhanced by temperature. All these aspects will be discussed hereafter on the basis of combining DIC analysis and high magnification SEM micrographs.

3.2. Influence of temperature on deformation mechanisms and their interactions

3.2.1 General context

Viscoplasticity of polycrystalline metals and alloys involves several microphysical mechanisms acting in volume, such as twinning and crystal slip, or at interfaces and grain boundaries, such as grain boundary sliding and/or migration. At high temperatures, crystal slip is combined with recovery processes such as dislocation climb, polygonization and dynamic recrystallization, which are controlled by volume diffusion. For fine grain sizes (typically less than 10 μm), high homologous temperatures and low strain rates, grain boundary sliding controlled by diffusional mass transfer may become the dominant mechanism [38]. The different mechanisms may operate simultaneously and their respective contributions to the overall strain depend on the thermodynamic and loading conditions (e.g. temperature, stress and/or strain rate magnitudes, chemical environment), but also on the microstructure (grain size and morphology, texture, second phases). For a given material and conditions, one may determine the dominant mechanisms on the basis of the widely used concept of deformation mechanisms maps, introduced in the 70s' [39], [40], [41]. However, the construction of such diagrams implicitly assumes that the considered mechanisms are independent, in other words that they act in parallel and contribute additively to the overall strain. This assumption is not straightforward, because simultaneously occurring mechanisms necessarily interact and some may possibly cooperate. As an example, in the case of dislocation creep ([42], [43]), strain mostly relates to crystal slip, but diffusion-controlled dislocation climb controls the overall steady-state creep rate. Another case is that of grain boundary sliding: substantial activity of grain boundary sliding can be observed for coarse-grained polycrystals even when, according to deformation mechanism maps, solely crystal slip should be promoted ([44], [45]). In fact, crystal plasticity is inherently anisotropic and the different slip systems are non-equivalent in terms of critical resolved shear stresses. Grain boundaries may therefore act as efficient barriers to slip transfer from a grain to another, thus inducing local plastic incompatibilities [16], [17], [18], [19]. Therefore, macro-homogeneous flow of polycrystals often involves not only crystal slip but also limited contribution of local accommodation mechanisms, such as grain boundary sliding [2], [3], ~~[46],~~ ~~[3]~~ and/or migration involving diffusional mass transfer or mobile disconnections [46~~1~~].

Mis en forme : Couleur de police : Rouge

Mis en forme : Couleur de police : Rouge

3.2.2. Deformation mechanisms at 110°C and 200°C

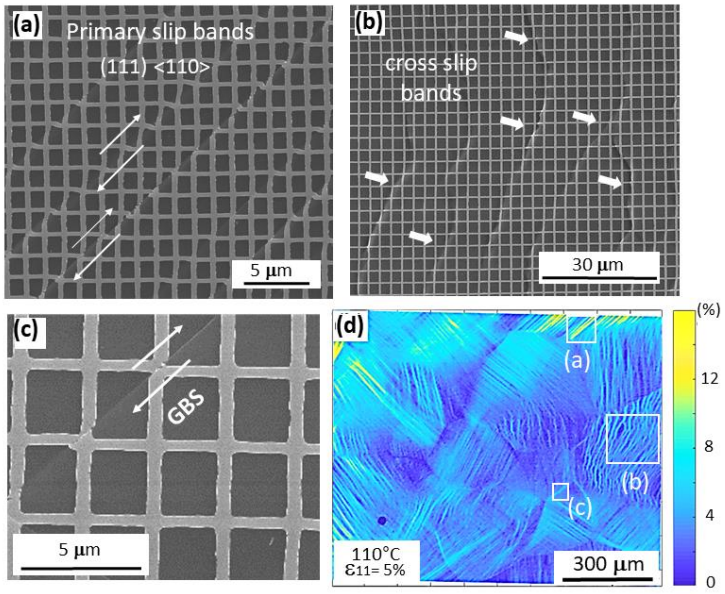

Figure 7: SEM and DIC characterization of deformation mechanisms at 110°C. (a) Straight slip bands: traces of (111)<110> primary slip (also called octahedral easy slip). (b) Wavy slip bands (traces of cross slip involving non-octahedral (112)~~(110)~~ <110> and (100)<110> slip). (c) Grain boundary sliding. Note that the sheared grid pattern indicates less than one micrometer GBS amplitude. (d) Equivalent strain map computed by DIC, indicating the areas exhibited in (a), (b) and (c). For instance, the presence of both DIC computed slip bands and respectively associated surface topography indicate both in-plane and out-of-plane slip components.

We clearly observe the occurrence of intra-granular and inter-granular deformation mechanisms. We will discuss at first the intra-granular plasticity mechanisms with respect to temperature and on the basis of the analysis of the active crystallographic slip systems. It is known from literature that at room temperature crystal plasticity of FCC metals occurs essentially by dislocation glide in the dense (111) octahedral crystallographic planes along the dense <110> crystallographic directions [47]. The primary (111) <110> "easy" slip system is sometimes called "octahedral" slip system. More specifically for aluminum, the primary (111) <110> slip systems are also the most active at moderate to intermediate temperatures (100 - 200°C). Metallographic and microstructural investigations showed that primary (111) <110> slip resulted in straight slip traces [48], [49]. But, at these temperatures gliding of dislocations in "non-octahedral" (100) (cubic) and (110) (dodecahedral) crystallographic planes becomes non-negligible [48], [49]. The activation of the cubic slip system results in wavy slip traces, interpreted as evidence of unstable slip on (100) planes and subsequent cross-slip occurring between the cubic system and two octahedral systems. In fact, cubic slip operates by kink-pair mechanism on screw dislocations, which dissociate in two

Mis en forme : Couleur de police : Rouge, Barré
Mis en forme : Couleur de police : Rouge
Mis en forme : Couleur de police : Rouge
Mis en forme : Couleur de police : Rouge
Mis en forme : Couleur de police : Rouge

intersecting (111) planes with low Schmid factors [48]. The resulting cross-slip is active enough to drastically influence the mechanical response and texture development in aluminum and aluminum alloys deformed at intermediate temperatures [48]. Such behavior is also reported in for other FCC metals (copper, silver and nickel), where dislocations gliding in (100) planes can dissociate in two intersecting (111) planes, independently of their different stalking fault energies [47]. More generally, thermally activated non-octahedral slip and resulting cross-slip in various FCC metals is documented in the literature [50], [51], [52], [53], [54], [55].

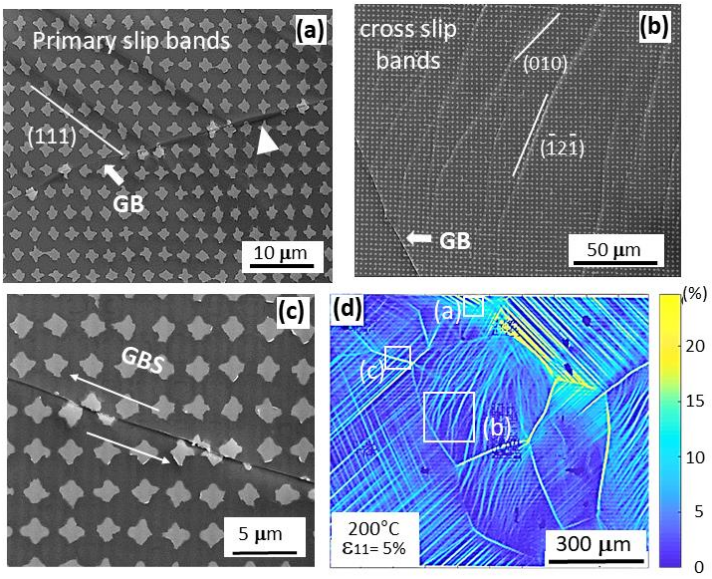

Figure 8: SEM and DIC characterization of deformation mechanisms at 200°C. (a) Straight slip bands: traces of (111)<110> primary slip (also called octahedral easy slip). The triangular arrow indicates considerable out-of-plane slip of one band along the grain boundary GB pointed by the common arrow. (b) Wavy slip bands (traces of cross slip involving non-octahedral (112)~~(110)~~ <110> ~~(110)~~ and (100)<110> slip). (c) Grain boundary sliding with several micrometers amplitude (note the sheared cross-like markers). (d) Equivalent strain map computed by DIC, indicating the positions of the areas exhibited in (a), (b) and (c). Note that GBS activity is much more pronounced than in Fig. 7.

We analyzed the crystallographic slip systems activated at moderate and intermediate temperatures based on i) the crystallographic orientation of individual grains (obtained by EBSD), ii) the geometrical analysis of the surficial slip bands (traces of active crystallographic slip planes intersecting the observation plane), iii) the hypothesis of the Schmid's law to determine the crystallographic slip direction providing the highest resolved shear stress in the previously identified slip plane. Octahedral slip (111) <110> is clearly identified, with slip traces characterized by

Mis en forme : Couleur de police : Rouge

Mis en forme : Couleur de police : Rouge

Mis en forme : Couleur de police : Rouge

Mis en forme : Couleur de police : Rouge

straight, sharp and very extended slip bands (Fig. 7a, Fig. 7d, Fig. 8a, Fig. 8d). Non-octahedral slip systems (100) <110> and (112) <110> are identified as involved in cross-slip, which results in wavy slip bands (Fig. 7b, Fig. 7d, Fig. 8b, Fig. 8d). In addition, ~~[55]~~ [49] reports that at high temperature the cubic slip becomes easy and stable, thus resulting in straight slip traces. In agreement with ~~[55]~~ [49], we do observe that at 300°C (and 400°C) all the slip traces become straight (Fig. 5d and 6f). In general, our observations of the morphology of slip bands shown in Fig. 5, Fig. 6, Fig. 7 and Fig. 8 and the identification of active slip systems by geometrical analysis of slip traces are in agreement with previous studies.

Recovery processes such as formation of dislocation walls and sub-grain boundaries involve dislocation climb and are therefore slowed down at moderate temperatures. As a result, dislocation densities increase. Gliding dislocations from different slip systems are mutually pinning which induces strain hardening (Fig. 4d). Conversely, at higher temperatures (200°C) dislocation climb processes are active, thus allowing for recovery and limited strain hardening (Fig. 4d). Therefore, crystal slip may be efficiently localized within fewer highly active slip bands, which seems to be the case when comparing Fig. 7d and 8d. Our observations are in agreement with previous works on aluminum crystal plasticity, which report that critical resolved shear stress, strain hardening and density of slip bands decrease with increasing temperature [56]. Interestingly, qualitatively similar observations are reported for DIC analysis of slip band density and their slip intensity in FCC ionic NaCl single crystals deformed at room temperature and high temperature [57].

Our study shows that GBS activity is low at 110°C (Fig. 7c), but becomes considerable at 200°C (Fig. 8c), which is in agreement with the general consensus that GBS is a thermally activated process. In the following we will focus on the data at 200°C and discuss the activation and interaction of crystal slip and GBS. Fig. 9a to Fig. 9d show the cumulative development of strain localization at four loading steps corresponding respectively to ca. 0.3%, 1.5 %, 3% and 5% macroscopic shortening. We can see in Fig. 9a that early strain localization occurring just after yielding (ca. 0.3% axial strain) corresponds simultaneously to crystal slip and GBS. The hollow arrow points to early GBS, whilst the solid arrow points to the trace of a slip band resulting from octahedral (111) <110> initially directly aligned with the mentioned sliding grain boundary. At this very early stage of deformation all crystal slip phenomena involve only octahedral slip systems (111) <110>, as evidenced by geometrical identification of (111) slip traces. The octahedral slip is characterized by sharp and straight slip bands crossing nearly the entire grains, like $\mathbf{g_1}$ (as defined in Fig. 6b and Fig. 9b). At about 1.5 % axial strain (Fig. 9b), localization patterns clearly affect all of the grains, combining both crystal slip and GBS. Some grains like $\mathbf{g_2}$ will be called “unfavorably oriented grains”, because their orientation with respect to the loading direction does not allow to activate extensive octahedral slip (low Schmid factors). Two such grains are present in the central part of Fig. 9b: $\mathbf{g_2}$ and $\mathbf{g_3}$. They develop numerous wavy slip bands, which indicate that their deformation is achieved by cross slip, owing to the activation of multiple non-octahedral slip systems, (100) <110> and (112) <110>.

Mis en forme : Couleur de police : Rouge, Barré

Mis en forme : Couleur de police : Rouge, Barré

Mis en forme : Couleur de police : Rouge

Mis en forme : Couleur de police : Rouge

The equivalent strain maps shown in Fig. 9c and Fig. 9d correspond respectively to ca. 3% and 5% The increasing overall strain results in increasing density and intensity of slip bands in all grains. Double octahedral slip activates in "favorably" oriented grains (which have high Schmid factors for (111) <110> primary slip systems), whilst cross-slip intensifies within "unfavorably" oriented ones (which have too low Schmid factors for (111)<110> primary slip systems and must activate non-octahedral slip systems, such as the cubic slip (100)<110> system). It is noteworthy that plastic compatibility between neighboring grains (e.g. g_2 and g_3) involves simultaneously both transmission of crystal slip across their boundaries and GBS. DIC offers the possibility of more detailed quantitative analysis of the respective contributions of both mechanisms [~~4~~6]. However, this is beyond the scope of the present work and will be addressed elsewhere.

Mis en forme : Couleur de police : Rouge

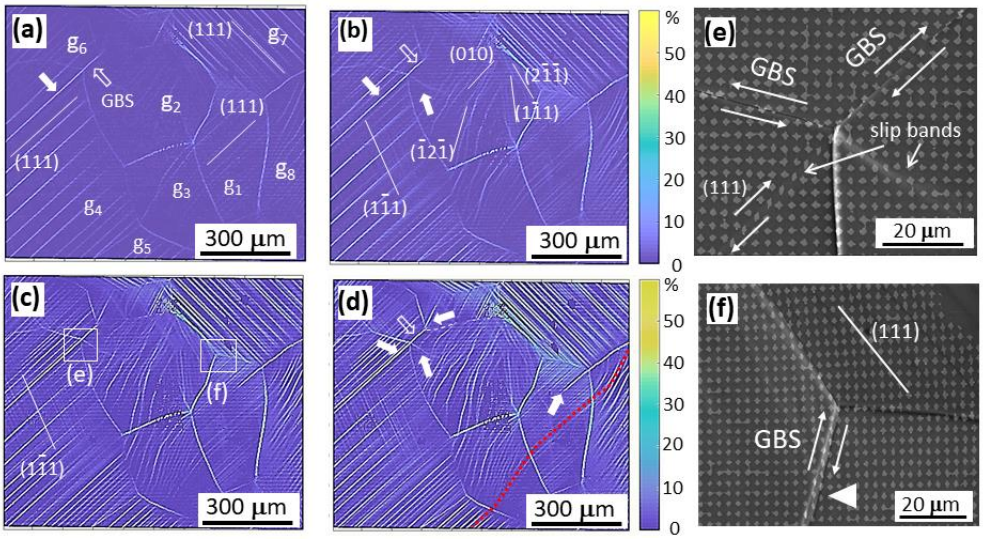

Figure 9: SEM and DIC characterization of deformation mechanisms at 200°C. (a), (b), (c) and (d) show the cumulative evolution of localization patterns at respective axial strains of ca. 0.3 % (briefly after yielding), 1.5, 3, and 5, respectively. Straight slip bands correspond to octahedral slip. Wavy cross slip bands represent cross-slip involving octahedral and non-octahedral slip. Crystal slip transmitted across four neighboring grains is underlined by one red doted trajectory. Hollow arrows point to GBS localization. Plain arrows indicate crystal slip bands aligned with grain boundaries subjected to GBS. The square-areas defined in (c) correspond to the SEM micrographs in (e) and (f), where the interactions between GBS and crystal slip at triple junctions is evidenced. In (e) the right hand GBS triggers on the left hand one octahedral (111) slip band. The left hand GBS triggers an undetermined crystal slip band on the right hand.

It is interesting to note that intense slip bands originate from triple junctions facing sliding grain boundaries, as indicated by solid arrows in Fig. 9a, 9b, 9c and 9d. Most triple junctions are concerned with more than one sliding grain boundary. Therefore, they may exhibit more than one originating slip band, each facing an adjacent sliding grain boundary. In fact, when GBS is active accommodation mechanisms are needed at triple junctions, where the third grain facing the sliding grain boundary may oppose the GBS process. Accommodation mechanisms may operate by local diffusional mass transfer and/or grain boundary migration [58], [59]. Micro-damage and cavitation at triple junctions may also occur, but the net result would be dilatant behavior [2], [60]. Conversely, localized slip bands may form in the third grain facing the sliding grain boundary. In Fig. 9a GBS is active at the grain boundary between g_2 and grain g_6 (indicated by hollow arrow). The third neighboring grain g_4 develops an intense slip band of primary slip system (111) <110> (indicated by plain arrow) in alignment with the sliding grain boundary between g_2 and grain g_6. Fig. 9b presents another similar interaction between GBS and crystal slip at the same triple junction between g_2, g_4 and g_6. GBS is activated between g_4 and grain g_6, whilst the slip band indicated by a second plain arrow develops in g_2. This triple junction is shown at higher magnification in the SEM micrograph in Fig. 9e. Both GBS and crystal slip interactions are clearly observed. Fig. 9f shows a case where GBS does not generate crystal slip band facing the sliding grain boundary. It is noteworthy that the GBS shows both in-plane and out-of-plane components (indicated by an arrow). The interactions between GBS and crystal slip are not straightforward. The cumulative DIC analysis may be ambiguous, because it does not show time resolved evolution of localization. Mechanisms activities and interactions may be better presented by incremental DIC analysis. Fig. 10a and Fig. 10b show respectively the incremental equivalent strain maps between steps 2 and 1, and steps 8 and 7, both corresponding to ca. 0.5 % increment of axial strain. It is observed that the activity of crystal slip is discontinuous with time. Some previously activated GBS or slip bands may have periods of inactivity, then reactivate later on. For example, in Fig. 10 the solid and dashed line ellipses show respectively the position of intermittent localization for both GBS and CSP, the dashed line ellipses/circles denoting the lack of activity previously indicated by the solid line ellipses/circles. The cumulative strain localization exhibited in Fig. 9c corresponds to step 8 (about 3% axial shortening) with reference to the initial state. It shows several grains where i) the spatial distribution of slip bands, ii) the intensity of individual slip bands are nearly homogeneous. The localization pattern shown in Fig. 10b also corresponds to step 8, but with reference to the state in step 7. Incremental DIC analysis clearly demonstrates that the activities of crystal slip and GBS mechanisms are not monotonously increasing with the macroscopic strain. Instead, we observe intermittent contributions of each mechanism, which could indicate local fluctuations of the stress state during the loading process. It also appears that octahedral slip triggers directly the formation of straight slip bands extending across the whole grain, whilst non-octahedral slip generates progressively extending cross-slip bands. This finding is in agreement with previous discussion about the unstable non-octahedral slip [48], [49].

Mis en forme : Couleur de police : Rouge

Mis en forme : Couleur de police : Rouge

Mis en forme : Couleur de police : Rouge

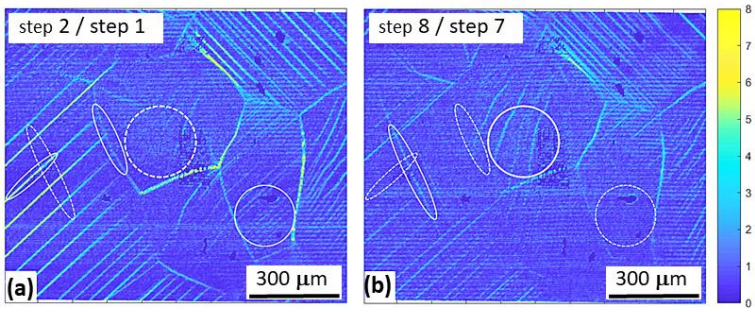

Figure 10: Incremental equivalent train maps of the sample shown in Fig. 9. (a) and (b) show the incremental evolution of localization with respect to the previous step of deformation as reference. Both maps correspond to an increment of ca. 0.5 % axial strain. Activity or inactivity of crystal slip and GBS are respectively indicated by solid line and dashed line ellipses/circles.

It is noteworthy that GBS amplitude varies along the sliding boundaries with maximum intensity in the central part of the grain boundary, and lower intensities towards the ending triple junctions. Similar gradients of GBS activities along sliding interfaces were experimentally observed during tension of pure aluminum with columnar microstructure [18].

3.2.3. Deformation mechanisms at 300°C

At high temperature (300°C) all the grains present mostly straight and diffuse slip bands. Cross-slip is no more observed, which is in agreement with the observations of ~~[55]~~ [49]. The authors reported that at high temperature the cubic slip of aluminum becomes easy and stable, thus resulting in straight slip traces. In addition, all grain boundaries present very strong localization, related to grain boundary sliding (GBS, Fig. 5d and 6f). In this case, very large in-plane and out-of-plane sliding components are observed on SEM micrographs. Out-of-plane GBS induces the development of strong topography (several micrometers are measured by AFM measurements), and in some cases grain thrusting. In this case the surface marking pattern is partly lost due to grain overlapping. In other cases, the in-plane GBS component is so important that marking patterns are extremely stretched and damaged. For these reasons, the DIC computation of strain along grain boundaries obtained at 300°C might be considered only as a lower bound. It is worth noting that GBS is usually invoked for superplastic behavior and is mostly associated with small grain sizes of the order of a few tens of µm or less ([44], [58], [59], [61], [62]). In the present study we clearly evidence the intense activity of GBS in coarse-grained aluminum. Using similar techniques, a recent study identified GBS in columnar, coarse grained and high purity aluminum, subjected to *in situ* SEM traction ([18]). In spite of different experimental conditions, materials and microstructures, the consistency of the

Mis en forme : Couleur de police : Rouge, Barré

Mis en forme : Couleur de police : Rouge

Mis en forme : Couleur de police : Rouge

experimental observations suggests the ubiquity of GBS. However, at 300°C and above in addition to pronounced GBS we also observed important grain boundary migration (GBM), which we will discuss now.

GBM is observed in different situations. In static conditions, it is simply driven by interfacial tension forces related to grain boundary curvature and tends to reduce the corresponding interfacial free energy. It is therefore the fundamental mechanism enabling grain growth. In our case, the initial heat treatment at 500°C did reset the preexisting texture inherited from the rolling process and substantial grain growth took place (Fig. 2). Chemical potential gradients and inter-diffusion processes across the interface between compounds (and alloys) may also induce GBM. The related phenomenon is either called chemically-induced or diffusion-induced GBM [63], [64], [65], [66]. However, this situation does not correspond to our case, since we have a nearly pure single-phase material. Conversely, along with dynamic recrystallization by sub-grain rotation, GBM is also reported as an efficient recovery mechanism. GBM is reported as the dominant restoration mechanism in severely deformed copper [67]. For hot-deformed polycrystals, dislocation-related elastic strain energies may differ across the boundaries of neighboring grains. GBM allows low-strained grains, or newly nucleated strain-free grains, to grow at the expense of older and heavily strained grains [68], [69], [70], [71], [72], [73], [74].

Mis en forme : Couleur de police : Rouge

Mis en forme : Couleur de police : Rouge

Mis en forme : Couleur de police : Rouge

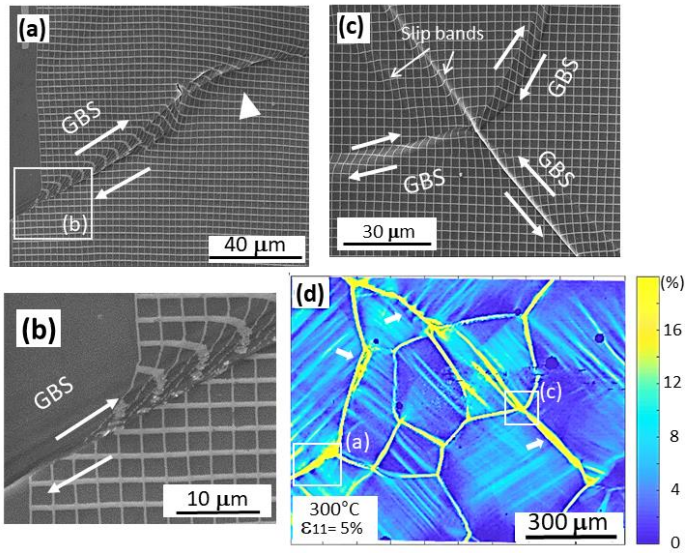

Figure 11: SEM and DIC characterization of deformation mechanisms at 300°C. (a) and (b) show a very intense GBS mechanism corresponding to the lower left-hand area indicated on the equivalent strain map in (d). The plain arrow in (a) show a wavy morphology of the grain boundary ahead of the intensely sliding portion shown in (b).

This curvature corresponds to a GBM mechanism. (c) shows the case of a triple junction, where GBS induces an intense slip band in the third grain facing the sliding boundary (like in Fig. 9e).

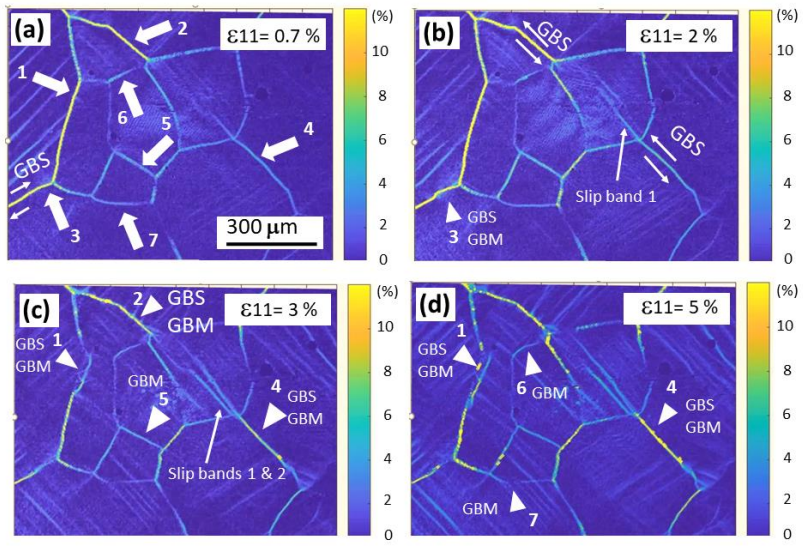

Figure 12: Incremental DIC analysis of the sample deformed at 300°C and shown in Fig. 10. The presented four loading stages take in account the previous loading step as reference, which allows to see the local evolution of mechanism activities as a function of time. In (a) the plain arrows point to different grain boundaries which present GBS or couples GBS and GBM. The grain boundary labelled "3" shows GBS in (a) and GBM in (b), as evidenced by the wavy morphology that develops in the originally straight grain boundary. This wavy character is previously presented in Fig. 11a. (b) also shows the intense slip band developing in relation to GBS, which was previously shown in Fig. 11c. In (c) wavy geometry develops at grain boundary "1" evidencing GBM, while coupled GBS and GBM activates at grain boundaries "2" and "3", as evidenced by the change of grain boundary curvature. Note that the sliding grain boundary "3" triggers a second slip band in the facing grain. The grain boundary "5" has also clearly migrated upwards, as does in (d) the grain boundary "7" of the same grain, which migrates downwards. In (d) the upwards evolution of the curvature of grain boundary "6" also shows GBM. Note that GBM is still active at the grain boundaries "1" and "4". The first, partly migrates backwards, while the second becomes very straight.

In our case of low strain GBM is not observed up to 200°C. It happens moderately at 300°C (Fig. 11 to Fig. 15), but starts to be very active at 400°C. Interestingly, the surface marking grid remains preserved during GBM, which confirms solely underlying diffusive mass transfer mechanisms. DIC is inherently suited to low strain and modestly evolving microstructures. Conversely, marked GBM is associated with strong evolution of the starting microstructure, which may complicate the DIC analysis. We already discussed the differences between cumulative and incremental DIC analysis (Fig. 9 and Fig. 10). When considering the cumulative strain with respect to the initial state as reference, GBM results in widely spread localization along the migrating portions of the sliding grain

boundaries, as shown in Fig. 11. It can be seen in Fig. 11a and Fig. 11b that a part of a grain boundary subjected to very strong GBS is affected by GBM (highlighted by a plain arrow), which induces a wavy interface.

The cumulative equivalent strain map shown in Fig. 11d shows that the latter GBM acts as a very spread interfacial localization. Several other interfaces affected by the same phenomenon are indicated by plain arrows. The step-by-step incremental DIC analysis presented in Fig. 12 demonstrates unambiguously the corresponding GBM mechanisms at work. In Fig. 12a plain arrows indicate specifically numbered grain boundaries, which are shown in Fig. 12b, Fig. 12c and Fig. 12d to activate GBS and/or GBM. The incremental DIC analysis evidences that at different times of the loading history the specified grain boundaries change their position and their curvature. Fig. 13, Fig. 14 and Fig. 15 show in more detail SEM micrographs of some of these mobile grain boundaries.

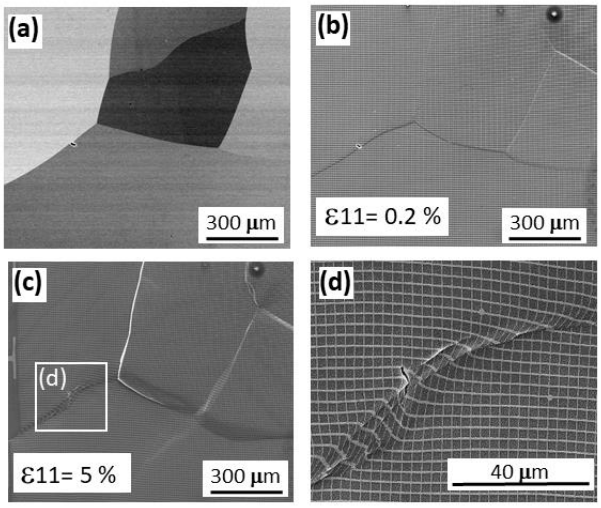

Figure 13: SEM micrographs of selected areas where GBS and/or GBM are simultaneously active at 300°C. (a) BSE mode image of the initial local microstructure next to the grain boundaries "3" and "7" shown in Fig. 12. (b) and (c) correspond to the same microstructure at two distinct loading stages, the first just after yielding and the second at the end of the test. Note the clear migration of boundaries "3" and "7". In (c) and (d) (at higher magnification) the development of a wavy geometry is observed along the simultaneously sliding and migrating grain boundary "3", with an upward migration portion (see also Fig. 12). Note that the boundary "7" has largely migrated downwards, similarly to the boundary of the left-hand neighboring grain.

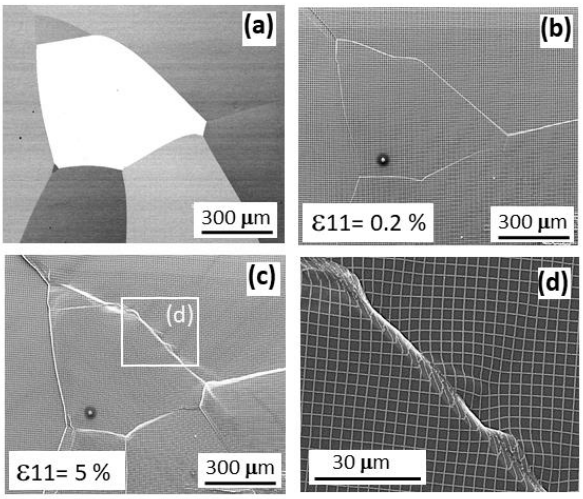

Figure 14: SEM micrographs of selected areas where GBS and/or GBM are simultaneously active at 300°C. (a) BSE mode image of the initial local microstructure next to the grain boundaries "2" and "6" shown in Fig. 12. (b) and (c) correspond to the same microstructure at two distinct loading stages, the first just after yielding and the second at the end of the test. Note the wavy migration of boundary "2". In (c) and (d) (at higher magnification) the development of a wavy geometry is observed along the simultaneously sliding and migrating grain boundary "2" (see also Fig. 12).

It is noteworthy that the GBS activity of the grain boundary "4" triggered two intense crystal slip bands in the grain facing the sliding boundary (Fig. 11 and Fig. 12), but as evidenced in Fig. 12b and Fig. 12c these bands (labelled band 1 and band 2) were activated sequentially, and present different orientations. This sequential evolution might be related to the simultaneous GBS and GBM (shown in Fig. 15). The migration of the grain boundary "4" modifies the interfacial angles at the triple junction, and hence the incidence of the sliding boundary with respect to the facing grain. This case of simultaneous coupling between GBS, GBM and crystal slip accommodation may be considered as an example of evolution of the local stress state, with respect to the evolution of microstructure and interactions of coexisting mechanisms.

GBM may operate at small scales and strains, being coupled with limited relative grain displacement, which is known as shear coupled GBM. All the experimental and numerical studies addressing this mechanism are based on TEM observations and atomistic scale simulations of particular grain boundaries. The involved grain boundary defects are called disconnections and are also operational at low temperature [75], 76], [77], [78]. While being an important phenomenon involved in dynamic recrystallization and grain growth processes in polycrystalline materials, GBM in itself is beyond the scope of this study and we will not elaborate further on it.

Mis en forme : Couleur de police : Rouge

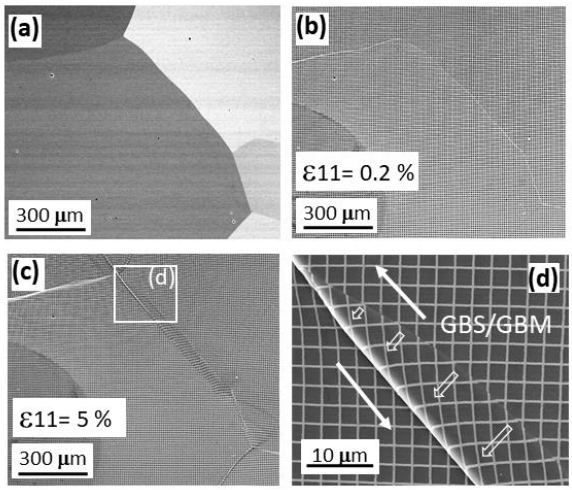

Figure 15: SEM micrographs of selected areas where GBS and/or GBM are simultaneously active at 300°C. (a) BSE mode image of the initial local microstructure next to the grain boundary "4" shown in Fig. 12. (b) and (c) correspond to the same microstructure at two distinct loading stages, the first just after yielding and the second at the end of the test. Note in (d) that the grain boundary "4" is initially smoothly curved upwards, but in (c) it is nearly straight. In (d) the result of simultaneous GBS and GBM mechanisms is seen at higher magnification. (see also Fig.12).

3.3. Subsurface microstructures investigated by FIB and TEM

The in situ SEM investigations give access to surface kinematic analysis, but the 3D microstructure in depth remains unknown. The observed surface traces of slip systems and the crystallographic orientations of the individual grains obtained by EBSD allow to identify the active slip planes. Active slip directions may be obtained by additional geometric analysis of most favorable Schmid factors, based on determination of resolved shear stresses with respect to the applied uniaxial stress (see previous section and Fig. 8 and Fig. 9). Conversely, geometrical analysis of GBS in terms of resolved shear stresses is difficult because the inclination of the GB plane in depth is unknown. Numerous grain boundary planes are slanted within the 3D microstructure, which is demonstrated by the observed out of plane sliding components.

Sophisticated techniques such as DCT (diffraction contrast tomography) give access to the 3D crystallographic microstructure, which reliably match with the surficial EBSD data ([79]). These techniques need however access to synchrotron radiation. Furthermore, their spatial resolution is poorer with respect to SEM and TEM, which precludes the identification of structural crystallographic defects along grain boundaries that may be involved in the GBS phenomenon. We therefore tried to capture some aspects of sliding interfaces using FIB

Mis en forme : Couleur de police : Rouge

(focused ion beam) machining and *post mortem* TEM investigations, in order to characterize grain boundary morphology at depth and dislocation microstructures in their vicinity.

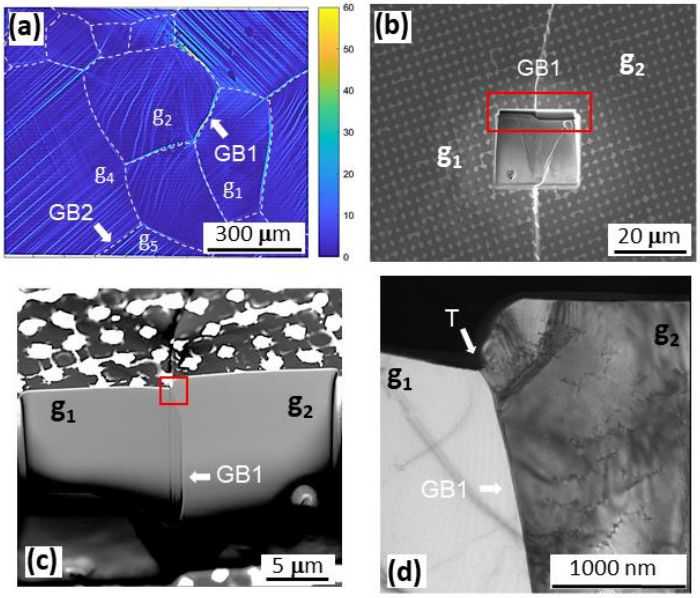

Figure 16: FIB milling of thin sections for TEM investigations. (a) Final equivalent strain map of the sample shown in Figures 6, 8, 9 and 10. The grain boundaries between grains g1 and g2 and between grains g4 and g8, that we call GB1 and GB2 show respectively important and little GBS activity. (b) GB1 is observed in the dual beam SEM-FIB. The excavation at the central part of the interface is operated by FIB milling. (c) Imaging of the cross section of the grain boundary from aside (tilted specimen). Note that GB1 is nearly vertical at depth, except in the very vicinity of the surface, where it is moderately inclined to the left. The straight vertical trace within grain g1, starting at the trace of GB1 on the sample surface, is due to a milling defect. (d) TEM bright field micrograph from a thin slice taken by FIB-machining from the near surface region of the GB (shown in (c) by the red frame). Grain g1 which activated only primary octahedral slip (Fig. 9) appears free of crystal defects in the vicinity of the grain boundary. Conversely, g2 activated octahedral and non-octahedral systems resulting in cross slip. It shows substantially high density of free dislocations, entangled dislocations and dislocation arrays. T is the surficial triple point representing the GB trace in the SEM observation plane.

We used focused ion beam (FIB Helios-660) to mill small volumes of about 100 μm^3 around specific grain boundaries of interest, where GBS was identified (Fig. 8, Fig. 9). The excavation allows to reveal the geometry of the GB at depth, and in particular its inclination. We observed that grain boundaries presenting essentially in-plane sliding are nearly perpendicular to the observation plane. An example is the grain boundary GB1 between grains g_1 and g_2, as shown in Fig. 16b and Fig. 16c. In Fig. 16d, Fig. 17 and Fig. 18a we show TEM micrographs of the

vicinity of GB1. Fig. 8 and Fig. 9 show that grains g_1 and g_2 present substantial differences in terms of localization patterns, which correlate differences in crystal plasticity mechanisms. Grain g_1 activated only primary octahedral slip, whilst grain g_2 activated cross-slip involving both octahedral and non-octahedral slip. It is therefore expected to observe more complex and entangled dislocation microstructures in g_2. In Fig. 16d, Fig. 17 and Fig. 18a, we show TEM micrographs from the uppermost part of the grain boundary GB1 (corresponding to the red frame in Fig. 16c). We can see, at the triple point T between g_1, g_2 and the free surface, the bulging of grain g_2 with respect to grain g_1, which may be simply due to thermal grooving of the grain boundary, or it may represent a small amount of out-of-plane GBS. The most interesting observation is the lack of inherited dislocation microstructures in g_1, whilst g_2 presents both numerous free dislocations and several complex dislocation arrays.

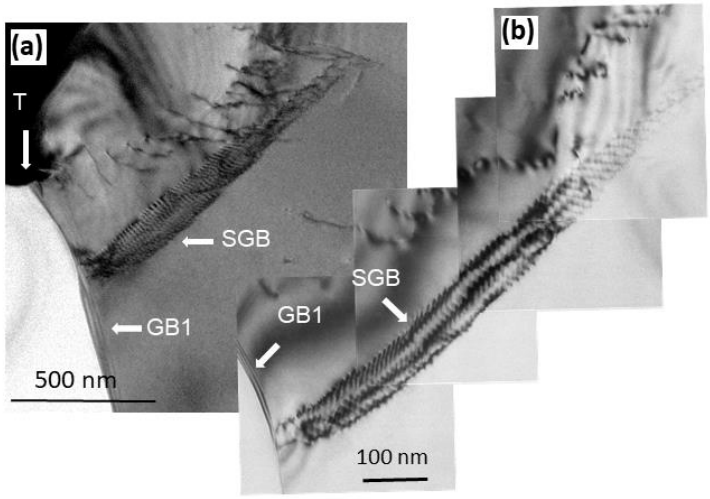

Figure 17: Higher magnification TEM micrographs from the same thin section as in Figure 16d. (a): The sub-grain boundary (SGB) in g2 is initiating at the grain boundary GB1 between grains g1 and g2 (Fig. 16a). T is the surficial triple point representing the intersection of GB1, the SEM observation plane and the TEM observation plane. It is a source of free dislocations gliding in grain g2 ~~towards the sub-grain boundary SGB. The triple junction T is the source of a series of free dislocations~~, piling up at the SGB. b: The SGB is shown in more detail, evidencing two sets of constitutive dislocation families.

Mis en forme : Couleur de police : Rouge, Barré

Mis en forme : Couleur de police : Rouge, Barré

Fig. 17 focuses on the area of the triple point T, at the top of GB1. Fig. 13a shows numerous dislocations emitted from T and gliding towards a sub-grain boundary (SGB) composed of two sets of parallel dislocations (Fig. 17b). The curved character of the dislocation lines indicates mixed edge and screw types of dislocations. This

observation is in agreement with the previous analysis of surface slip bands evidencing cross-slip. The striking difference of dislocation microstructures on either side may indicate the plastic incompatibility between the two grains as a reason for GBS activation. In addition, we observed that GB1 migrates slightly at the expense of g_2. The migration is demonstrated by the curvature of GB1 in the vicinity of the sample surface, whilst it remains straight and vertical at depth (Fig. 16c). It is reported in literature that thermal grooving of grain boundaries may significantly affect grain growth in the vicinity of free surfaces. The triple junctions (T) of the grooved grain boundaries may pin moving grain boundaries [80], [81], hence inducing characteristic sub-surface curvatures boundaries, as shown in Fig. 16c. As discussed in the previous section, GB1 migration between g_1 and g_2 may be seen as the result of the different dislocation densities on either side and corresponding strain energies. The intimate mechanism involved in the GBS itself still remains unclear. Yet, in the present case at 200°C, we cannot exclude contribution of disconnections to the simultaneous GBS and fine scale GBM [76], [77], [78].

Mis en forme : Couleur de police : Rouge

Mis en forme : Couleur de police : Rouge

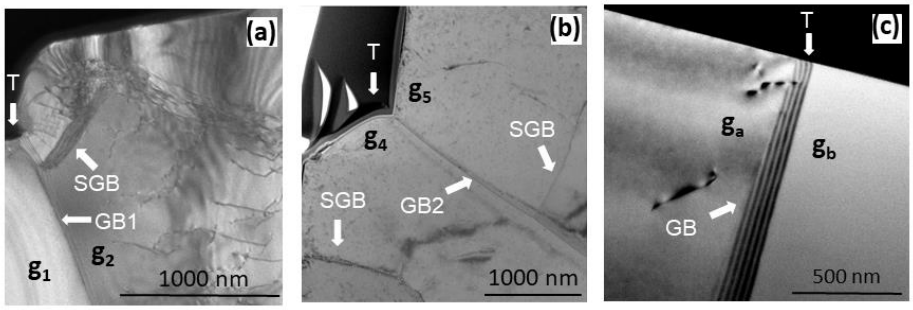

Figure 18: TEM micrographs from the vicinity of selected grain boundaries. (a) and (b) Respectively, vicinity of GB1 and GB2 (Fig. 16a). Dislocation densities strongly differ on either side for GB1 (strongly affected by GBS), but for GB2 (little affected by GBS). (c) Vicinity of grain boundary GB between grains g_a and g_b in a starting material. The sample is not deformed and heat-treated after polishing, hence there is no surface grooving at the triple point T. Very few free dislocations are observed. Note that the GB is not perfectly oriented edge-on, and is showing fringes indicative of the slice thickness.

We further observed by TEM similar bi-crystalline lamellae, extracted from grain boundaries of undeformed starting aluminum, or from grain boundaries of exhibiting little GBS, like GB2 between g_4 and g_8 (Fig. 16a). We compare in Fig. 18 the dislocation microstructures corresponding to GB1, GB2 and one grain boundary from a starting undeformed material. Fig. 18a shows the contrasting microstructures on either side of GB1. Fig. 18b shows similar dislocation microstructures in g_4 and g_8. They both display sub-grain boundaries and fewer free dislocations. Both grains activated primary octahedral slip, leaving extended straight surface traces (Fig.

8, Fig. 9, Fig. 16). The latter traces are nearly aligned, suggesting that g_4 and g_8 are plastically compatible, which might be the reason why GB2 shows very little GBS. Fig. 18c shows that the grain boundary area of the starting undeformed material is nearly dislocation-free. Note that the triple point T does not present surface grooving.

Our observations do not determine unambiguously the working mechanisms of the GBS phenomenon. We report simultaneous moderate GBS and minor GBM at 200°C, which may indicate a contribution of disconnections [76], [77], [78]. In the same time, we observed considerable dislocation microstructures, therefore dislocation activity at sliding grain boundaries may also be involved. It is admitted now that specific dislocation mechanisms occur at grain boundaries and movements of dislocation inside the grain boundaries have been observed. Apart from movement of single dislocations, we should also consider more complex assemblies, such as pile-ups at the grain boundary, which have been pointed out by DDD (discrete dislocation dynamics) studies coupled to Laue micro-diffraction experiments ~~[82)~~ [82]. Such dislocation structures initiating at a sliding grain boundary may be at the origin of sub-grain boundaries such as the one we report in Fig. 17. Our micrographs drive at exploring more boundaries, which can be an incentive to envisage additional dislocation microstructures at grain boundaries. Conversely, the considerable GBS and major GBM that we observed at 300°C might involve substantial diffusional mass transfer. It is likely that all these mechanisms may participate in the GBS mechanism, with respective contributions depending on the temperature, loading conditions, neighboring grain disorientation and local grain boundary geometry. Further *in situ* investigations at TEM scale might be necessary to discriminate among these numerous options.

Mis en forme : Couleur de police : Rouge

Mis en forme : Couleur de police : Rouge, Barré

3.4. Conclusions

We performed multi-scale investigation of the micromechanical behavior of nearly pure coarse grained aluminum, using hot compression tests *in-situ* SEM and full-field measurements by DIC analysis. The localization patterns allowed to discriminate the deformation mechanisms active at 25°C, 110°C, 200°C and 300°C and at constant strain rate of about 10^{-5} s^{-1}. Deformation was largely dominated by crystal slip. At room temperature, localization occurs exclusively as extended straight slip traces, evidencing primary octahedral (111)<110> slip. At moderate and intermediate temperatures octahedral slip is complemented by non-octahedral slip (i.e. cubic (100) <110> and (112)<110>), which results in cross-slip as evidenced by additional wavy slip traces.

The DIC analysis evidenced substantial localization at grain boundaries, which progressively activate GBS with increasing temperature. GBS starts modestly slightly above 100°C, but becomes substantial at 200°C. The puzzling observation is that GBS activates as soon as primary octahedral slip, at axial strains of less than half a percent, and continues to be active all along the deformation process. Both mechanisms continuously interact, for instance at triple junctions, where pronounced GBS triggers intense crystal slip bands in the grains facing the sliding boundary.

Owing to *in situ* full-field measurements by DIC analysis and TEM investigations of *post mortem* dislocation microstructures, GBS intensity seems to correlate with the extent of crystal slip incompatibility of neighboring grains. These observations suggest that both mechanisms are mutually accommodating each other. Incremental full-field measurements allowed to evidence that at local scales crystal slip and GBS are both intermittently active, suggesting fluctuations of local stress states during the loading process. At 300°C and above GBS is prominent and often combined with important GBM. Strong out-of-plane GBS components result in the development of marked topography. GBM substantially remodel the interfacial morphology, sometimes facilitating the accommodation interactions between crystal slip and GBS at triple junctions.

Our conclusions are that moderate deformation of aluminum at intermediate temperatures (200°C – 300°C) relies on the interplay between multiple slip system based crystal plasticity, grain boundary sliding and grain boundary migration. The different mechanisms interacting on one another could participate to local fluctuations of stress and strain states so as to cope with the microstructural heterogeneities, and allow macro-homogeneous flow.

Funding: This work has been supported by the Fondation EDF, sponsoring the chair "Energies durables" under the supervision of Franck Carré.

Acknowledgements

We thank Vincent de Greef, Erik Guimbretière, Hakim Gharbi and Jean-Christophe Eytard for their precious technical support. We also warmly thank Romain Quey (Lab. George Friedel, Ecole des Mines de Saint-Etienne) for kindly providing the aluminum alloy and Eva Héripré (MSSMAT, Ecole Centrale Supelec) for access and help with the FIB.

Conflict of Interest Statement

On behalf of all authors, the corresponding author states that there is no conflict of interest.

References

[1] L. Allais, M. Bornert, T. Bretheau, and D. Caldemaison: Acta. Metall. Mater., 1994, vol. 42, pp. 3865-3880.

[1] N. Combe, F. Mompiou, and M. Legros: Phys. Rev. Mater., 2019, vol. 3, pp. 060601.

[2] M. Bourcier, M. Bornert, A. Dimanov, E. Heripre, and J.L. Raphanel: J. Geophys. Res. Solid Earth, 2013, vol. 118, pp. 511–526.

[3] V. Doquet and B. Barkia: Mech. Mat., 2016, vol. 103, pp. 18–27.

[4] L. Allais, M. Bornert, T. Bretheau, and D. Caldemaison: Acta. Metall. Mater., 1994, vol. 42, pp. 3865-3880.

[45] P. Doumalin and M. Bornert: Interferometry in Speckle Light, 2000, 67–74.

Mis en forme : Couleur de police : Rouge, Barré

Mis en forme : Retrait : Gauche : 0,51 cm, Première ligne : 0 cm, Interligne : Multiple 1,49 li

Mis en forme : Couleur de police : Rouge, Barré

Mis en forme : Couleur de police : Rouge, Barré

,DOI:10.1007/978-3-642-57323-1_9
[56] A. Goyal, V. Doquet, and A. Pouya,; Metall. Mater. Trans. A, 2020, vol. 51, pp. 1109-1122.
[7] Z. Song, R. Niu, X. Cui, E. V. Bobruk, M. Y. Murashkin, N. A. Enikeev, J. Gu, M. Song, V. Bhatia, S. P. Ringer, R. Z. Valiev and X. Liao: Acta Mat., 2023, vol. 246, 118671. DOI: 10.1016/j.actamat.2023.118671
[8] J. Dautriat, M. Bornert, N. Gland, A. Dimanov, and J.L. Raphanel: Tectonophysics, 2011, vol. 503, pp. 100-116.
[9] E. Héripré, M. Dexet, J. Crépin, L. Gélébart, A. Roos, M. Bornert, and D. Caldemaison: Int. J. Plast., 2007, vol. 23, pp. 1512-1539. https://doi.org/10.1016/j.ijplas.2007.01.009
[10] M.A. Sutton, N. Li, D.C. Joy, A.P. Reynolds and X. Li.: Exp. Mech., 2007, vol. 47, pp. 775-787. DOI: 10.1007/s11340-007-9042-z
[11] R. Quey, P. Dawson, and J.H. Driver: IOP Conf. Ser.: Mater. Sci. Eng., 2015, vol. 89, 012011.
[12] P. Doumalin, M. Bornert, and D. Caldemaison: Proc. Int. Conf. on Adv. Techn. Exp. Mech., JSME, 1999, vol. 1, pp. 81-86.
[13] P. Doumalin, P. and M. Bornert: in P. Jacquot, J.M. Fournier (Eds.), Proc. Interferometry in Speckle Light: Theory and Applications, Springer-Verlag, EPFL Lausanne, 2000, pp. 67-74.
[15] R. Quey, D. Piot and J.H. Driver: Acta Mater., 2010, vol. 58, pp. 1629-1642.
[16] T.R. Bieler, P. Eisenlohr, H.J. Phukan, and M.A. Crimp: Curr. Opin. Solid State Mater. Sci., 2014, vol. 18, pp. 212-226.
[17] T.R. Bieler, R. Alizadeh, M. Peña Ortega, and J. Llorca: Int. J. Plast., 2019, vol. 118, pp. 269-290.
[18] M.A. Linne, A. Venkataraman, M.D. Sangid, and S. Daly: Exp. Mech., 2019, vol. 59, pp. 643-658.
[19] R. Alizadeh, M. Peña Ortega, T.R. Bieler, and Llorca, J.: Ser. Mater., 2020, vol. 178, pp. 408-412.
[20] A. Mecif, B. Bacroix and P. Franciosi: Acta Mater., 1997, vol. 45, pp. 371-381.
[21] A. El Sabbagh : Thèse de Doctorat en Mécanique des Matériaux de l'Ecole Polytechnique, Palaiseau, 2018
[22] A.D. Kammers and S. Daly: Meas. Sci. Technol., 2011, vol. 22, pp. 125501. doi:10.1088/0957-0233/22/12/125501
[23] A.D. Kammers and S. Daly: Exp. Mech., 2013, vol. 53, pp. 1333-1341.
[24] Y. Zhang, T.D. Topping, E.J. Lavernia and S.R. Nut: Metall. Mater. Trans. A, 2014, vol. 45A, pp. 47-54. DOI: 10.1007/s11661-013-1805-9
[25] Barranger, Y., P. Doumalin, J. C. Dupré, and A. Germaneau: Strain, 2012, vol. 48(5), pp. 357-365. doi:10.1111/j.1475-1305.2011.00831.x
[26] P. Reu: Exp. Techn., 2014, vol. 38(5), pp. 1-3. doi:10.1111/ext.12111
[27] V. Doquet and B. Barkia: Mech. Mat., 2016, vol. 103, pp. 18-27.
[28] Y.L. Dong and B. Pan: Exp. Mech. 2017, vol. 57(8), pp. 1161-1181. doi:10.1007/s11340-017-0283-1.

Mis en forme

~~[29] M. Grédiac, B. Blaysat and F. Sur: Exp. Mech., 2020, vol. 60(4), pp .509-534. DOI:10.1007/s11340-019-00579-z~~

~~[30] X. Hu, Z. Xie and F. Liu: Measurement, 2021, vol. 173, 108618. https://doi.org/10.1016/j.measurement.2020.108618~~

~~[31] D. Boivin and P. Caron: J. Mater. Sci., 2010, vol. 45, pp. 5649-5659. DOI: 10.1007/s10853-010-4630-1~~

~~[32] G. Martin, C.W. Sinclair and J.-H. Schmitt: Scripta Mat., 2013, vol. 68(9), pp. 695-698. https://doi.org/10.1016/j.scriptamat.2013.01.017~~

~~[33] G. Martin, D. Caldemaison, M. Bornert, C. Pinna, Y. Bréchet, M. Véron, J.D. Mithieux and T. Pardoen: Exp. Mech. 2013, vol. 53(2), pp. 205-215. DOI:10.1007/s11340-012-9628-y~~

~~[34] K. Thibault, D. Locq, P. Caron, D. Boivin, Y. Renollet, Y. and Y. Bréchet, : Mat. Sci. Eng. A, 2013, vol. 588, pp.14-21.~~

~~[35] T. Dessolier, P. Lhuissier, F. Roussel-Dherbey, F. Charlot, C. Josserond, J-J. Blandin and G. Martin: Mat. Sci. Eng. A., 2020, vol. 775. 138957. https://doi.org/10.1016/j.msea.2020.138957~~

~~[36] Kammers, A.D. and S. Daly: Exp. Mech. 2013, 53(9), 1743–1761. DOI:10.1007/s11340-013-9782-x~~

~~[37] Weidner, A. and H. Biermann: Adv. Eng. Mat., 2021, 23(4) 2001409 https://doi.org/10.1002/adem.202001409~~

~~[38] M. Kawasaki. and T.G. Langdon: J. Mater. Sci., 2007, vol. 42, pp. 1782-1796.~~

~~[39] F. Ashby: Acta Metall., 1972, vol. 20, pp. 887-897.~~

~~[40] F. Ashby: Adv. Appl. Mech., 1982, vol. 23, pp. 117-177.~~

~~[41] H.J. Frost and M.F. Ashby: Deformation Mechanism. Maps: The Plasticity and Creep of Metals and Ceramics, Pergamon Press, Oxford, New York, 1982, 166 pp.~~

~~[42] J. Weertman: J. Appl. Phys., 1957, vol. 28, pp. 1185-1189.~~

~~[43] J. Weertman: J. Appl. Phys., 1957, vol. 28, pp. 362.~~

~~[44] H. Lüthy, R.A. White, and O.D. Sherby: Mat. Sci. Eng., 1979, vol. 39, pp. 211-16.~~

~~[45] B. Fazan, O.D. Sherby, and J.E. Dorn: J. Met., 1954, vol. 6, pp. 919-922.~~

~~[46] A. Gaye, M. Bourcier, M. Bornert, E. Héripré, A. Dimanov, J. Raphanel, and K. Sab: Am. Rock Mech. Assoc., ARMA, 2014, 48th US Rock Mechanics / Geomechanics Symposium, Minneapolis (USA).~~

~~[47] H.P. Karnathaler: Phil. Mag. A, vol. 38(2), 1978, pp. 141-156. https://doi.org/10.1080/01418617808239225~~

~~[48] M. Carrard and J.L. Martin: Phil Mag A, 1987, vol. 56(3), pp. 391-405.~~

~~[49] D. Caillard and J.L. Martin: Int. J. Mat. Res., 2009, vol. 100(10). pp. 1403-1410. DOI:10.3139/146.110190~~

~~[50] R. Le Hazif and J.-P. Poirier: Acta Metall., 1975, vol. 23, pp. 865-871.~~

Mis en forme : Couleur de police : Rouge, Français (France), Barré
Mis en forme : Couleur de police : Rouge, Barré
Mis en forme : Couleur de police : Rouge, Barré
Mis en forme : Couleur de police : Rouge, Barré
Mis en forme : Non souligné, Couleur de police : Rouge, Barré
Mis en forme : Couleur de police : Rouge, Barré
Mis en forme : Couleur de police : Rouge, Barré
Mis en forme : Couleur de police : Rouge, Barré
Mis en forme : Couleur de police : Rouge, Barré
Mis en forme : Couleur de police : Rouge, Barré
Mis en forme : Couleur de police : Rouge, Barré
Mis en forme : Couleur de police : Rouge, Barré
Mis en forme : Couleur de police : Rouge, Barré
Mis en forme : Couleur de police : Rouge, Barré
Mis en forme : Couleur de police : Rouge, Barré
Mis en forme : Couleur de police : Rouge, Barré
Mis en forme : Couleur de police : Rouge, Barré
Mis en forme : Couleur de police : Rouge, Barré
Mis en forme : Couleur de police : Rouge, Barré
Mis en forme : Couleur de police : Rouge, Barré
Mis en forme : Couleur de police : Rouge, Barré
Mis en forme : Couleur de police : Rouge, Barré
Mis en forme : Couleur de police : Rouge, Anglais (États-Unis), Barré
Mis en forme : Couleur de police : Rouge, Barré
Mis en forme : Couleur de police : Rouge, Barré
Mis en forme : Couleur de police : Rouge, Barré
Mis en forme : Couleur de police : Rouge, Barré
Mis en forme : Couleur de police : Rouge, Barré
Mis en forme : Non souligné, Couleur de police : Rouge, Barré
Mis en forme : Couleur de police : Rouge, Barré
Mis en forme : Couleur de police : Rouge, Barré
Mis en forme : Couleur de police : Rouge, Barré
Mis en forme : Couleur de police : Rouge, Barré
Mis en forme : Couleur de police : Rouge, Barré

[51] B. Bacroix, and J.J. Jonas: Texture, Stress, Microstruct., 1987, vol. 8, 957619.
[52] A. Couret and D. Caillard: Acta Metall., 1988, vol. 36, pp. 2515-2524.
[53] D. Caillard and J.L. Martin: J. Phys., 1989, vol. 50, pp. 2455-2473.
[54] A. Albou, A. Borbely, C. Maurice and J.H. Driver: Phil. Mag., 2011, vol. 91, pp. 3981-4000.
[55] D. Caillard and J. L. Martin: Int. J. Mater. Res., 2009, vol. 100, pp. 1403-1410.
[56] F.D. Rosi and C.H. Mathewson: JOM, 1950, vol. 2, pp. 1159-1167. https://doi.org/10.1007/BF03399117
[57] D. Picard, A. Dimanov, and J.L. Raphanel: Mat. Sci. Eng. A., 2018, vol. 732, pp. 284-297.
[58] M.F. Ashby and R.A. Verall: Acta Metall., 1973, vol. 21, pp. 149-63.
[59] R. Raj and M.F. Ashby: Metall. Trans., 1971, vol. 2, pp. 1113-1127.
[60] A. Dimanov, G. Dresen, E. Rybacki, and R. Wirth: J. Struct. Geol., 2007, vol. 29, pp. 1049-69.
[61] C.N. Ahlquist and R.A. Menezes: Mater. Sci. Eng., 1971, vol. 7, pp. 223-224.
[62] T.G. Langdon: Phil. Mag., 1971, vol. 21, pp. 689-700.
[63] M. Hillert *and* Gary R. Purdy: Acta Metall., 1978, vol. 26(2), pp. 333-340, https://doi.org/10.1016/0001-6160(78)90132-3
[64] M. Hillert: Scr Metall., 1983, vol. 17(2), pp. 237-240, https://doi.org/10.1016/0036-9748(83)90105-9
[65] R.W. Balluffi and J.W. Cahn: Acta Metall, 1981, vol. 29(3), pp. 493-500, https://doi.org/10.1016/0001-6160(81)90073-0
[66] D.L. Beke, Yu. Kaganovskii and G.L. Katona: Progress Mat. Sci., 2018, vol. 98, pp. 625-674.
[67] O. Renk, A. Hohenwarter, S. Wurster, and R. Pippan: Acta Mater., 2014, vol. 77(100), pp. 401-410, doi: 10.1016/j.actamat.2014.06.010J.
[68] J.E. Harris: Nature 200, 1963, p1197. https://doi.org/10.1038/2001197a0
[69] P. Duval and O. Castelnau: J. Phys. IV, 1995, vol. 05 (C3), pp. 197-205.
[70] M. Montagnat and P. Duval: Earth. Planet. Sci Lett., 2000, Vol., 183(1-2), pp. 179-186, DOI:10.1016/S0012-821X(00)00262-4
[71] M. Tonks, P. Millett, W. Cai and D. Wolf: Scripta Mat., 2019, vol. 63(11), pp. 1049-1052, https://doi.org/10.1016/j.scriptamat.2010.07.034
[72] S.B. Lee, J. Jung and H.N. Han: Materials, 2020 vol. 13(2), 360, https://doi.org/10.3390/ma13020360
[73] A. Lens, C. Maurice and J.H. Driver: Mat. Sci. Eng. A, 2005, vol. 403(1-2) pp. 144-153, https://doi.org/10.1016/j.msea.2005.05.010
[74] M.L. Taheri, D. Molodov, G. Gottstein and A.D. Rollett: Z. Metall., 2005, vol. 96, pp.1166-1170, DOI: 10.3139/146.101157
[75] A. Rajabzadeh, F. Mompiou, S. Lartigue-Korinek, N. Combe, M. Legros, M., and D.A. Molodov: Acta Mater., 2014, vol. 77, pp. 223-235.

Mis en forme : Couleur de police : Rouge, Anglais (États-Unis), Barré
Mis en forme : Couleur de police : Rouge, Barré
Mis en forme : Couleur de police : Rouge, Anglais (États-Unis), Barré
Mis en forme : Couleur de police : Rouge, Barré
Mis en forme : Couleur de police : Rouge, Barré
Mis en forme : Couleur de police : Rouge, Barré
Mis en forme : Couleur de police : Rouge, Barré
Mis en forme : Couleur de police : Rouge, Barré
Mis en forme : Couleur de police : Rouge, Barré
Mis en forme : Couleur de police : Rouge, Barré
Mis en forme : Couleur de police : Rouge, Barré
Mis en forme : Couleur de police : Rouge, Barré
Mis en forme : Couleur de police : Rouge, Barré

~~[76] N. Combe, F. Mompiou, M. Legros: Phys. Rev. B: Condens. Matter and Mater. Phys., 2016, vol. 93, pp. 024109.~~

~~[77] N. Combe, F. Mompiou, and M. Legros: Phys. Rev. Mater., 2019, vol. 3, pp. 060601.~~

~~[78] M. Larranaga, F. Mompiou, M. Legros, and N. Combe: Phys. Rev. Mater., 2020, vol. 4, pp.123606.~~

~~[79] N. Vigano, A. Tanguy, S. Hallais, A. Dimanov, M. Bornert, K.J. Batenburg, and W. Ludwig: Sci. Rep., 2016, vol. 6, pp.1–9.~~

~~[80] Y. Palizdar, D. San Martin, M. Ward, R.C. Cochrane, R. Brydson, and A.J. Scott: Mater. Charact., 2013, vol. 84, pp. 28–33.~~

~~[81] M. Verma, R. Mukherjee:. J. Appl. Phys., 2021, vol. 130, pp. 025305.~~

~~[82] G. Daveau : Thèse Ecole Centrale, Paris, 2012, https://tel.archives-ouvertes.fr/tel-00740650.~~

References

[1] L. Allais, M. Bornert, T. Bretheau, and D. Caldemaison: Acta. Metall. Mater., 1994, vol. 42, pp. 3865-3880.

[2] M. Bourcier, M. Bornert, A. Dimanov, E. Heripre, and J.L. Raphanel: J. Geophys. Res. Solid Earth, 2013, vol. 118, pp. 511–526.

[3] V. Doquet and B. Barkia: Mech. Mat., 2016, vol. 103, pp. 18-27.

[4] P. Doumalin and M. Bornert, M.: In: Jacquot, P., Fournier, JM. (eds) Interferometry in Speckle Light, 2000, Springer, Berlin, Heidelberg. Pp. 67-74. https://doi.org/10.1007/978-3-642-57323-1_9

[5] A. Goyal, V. Doquet, and A. Pouya,: Metall. Mater. Trans. A, 2020, vol. 51, pp. 1109-1122.

[6] A. Gaye, M. Bornert, N. Lenoir, K. Sab, A. Dimanov, M. Bourcier, E. Héripré, J.L. Raphanel, H. Gharbi, D. Picard, W. Ludwig: Am. Rock Mech. Ass., 2014, ARMA 14-7473.

[7] Z. Song, R. Niu, X. Cui, E. V. Bobruk, M. Y. Murashkin, N. A. Enikeev, J. Gu, M. Song, V. Bhatia, S. P. Ringer, R. Z. Valiev and X. Liao: Acta Mat., 2023, vol. 246, 118671. DOI: 10.1016/j.actamat.2023.118671

[8] J. Dautriat, M. Bornert, N. Gland, A. Dimanov, and J.L. Raphanel: Tectonophysics, 2011, vol. 503, pp. 100-116.

[9] E. Héripré, M. Dexet, J. Crépin, L. Gélébart, A. Roos, M. Bornert, and D. Caldemaison: Int. J. Plast., 2007, vol. 23, pp. 1512-1539. https://doi.org/10.1016/j.ijplas.2007.01.009

[10] M.A. Sutton, N. Li, D.C. Joy, A.P. Reynolds and X. Li.: Exp. Mech., 2007, vol. 47, pp. 775-787. DOI: 10.1007/s11340-007-9042-z

[11] R. Quey, P. Dawson, and J.H. Driver: IOP Conf. Ser.: Mater. Sci. Eng., 2015, vol. 89, 012011.

[12] P. Doumalin, M. Bornert, and D. Caldemaison: Proc. Int. Conf. on Adv. Techn. Exp. Mech., JSME, 1999, vol. 1, pp. 81-86.

[13] G. Martin, D. Caldemaison, M. Bornert, C. Pinna, Y. Bréchet, M. Véron, J.D. Mithieux and T. Pardoen : Exp. Mech., 2013, vol. 53(2). pp. 205-215. DOI:10.1007/s11340-012-9628-y

Mis en forme : Couleur de police : Rouge, Barré

Mis en forme : Couleur de police : Rouge, Barré

Mis en forme : Couleur de police : Automatique

Mis en forme : Couleur de police : Automatique

Mis en forme : Couleur de police : Automatique

[14] L. Wang, M. Bornert, E. Héripré, S. Chanchole and A. Tanguy: Strain, 2014, vol. 50(5), pp 370-380.
[15] R. Quey, D. Piot and J.H. Driver: Acta Mater., 2010, vol. 58, pp. 1629-1642.
[16] T.R. Bieler, P. Eisenlohr, H.J. Phukan, and M.A. Crimp: Curr. Opin. Solid State Mater. Sci., 2014, vol. 18, pp. 212-226.
[17] T.R. Bieler, R. Alizadeh, M. Peña-Ortega, and J. Llorca: Int. J. Plast., 2019, vol. 118, pp. 269-290.
[18] M.A. Linne, A. Venkataraman, M.D. Sangid, and S. Daly: Exp. Mech., 2019, vol. 59, pp. 643-658.
[19] R. Alizadeh, M. Peña-Ortega, T.R. Bieler, and Llorca, J.: Scr. Mater., 2020, vol. 178, pp. 408-412.
[20] A. Mecif, B. Bacroix and P. Franciosi: Acta Mater., 1997, vol. 45, pp. 371-381.
[21] A. El Sabbagh : Thèse de Doctorat en Mécanique des Matériaux de l'Ecole Polytechnique, Palaiseau, 2018.
[22] A.D. Kammers and S. Daly: Meas. Sci. Technol., 2011, vol. 22, pp. 125501. doi:10.1088/0957-0233/22/12/125501
[23] A.D. Kammers and S. Daly: Exp. Mech., 2013, vol. 53, pp. 1333–1341.
[24] Y. Zhang, T.D. Topping, E.J. Lavernia and S.R. Nut: Metall. Mater. Trans. A, 2014, vol. 45A, pp. 47-54. DOI: 10.1007/s11661-013-1805-9
[25] Barranger, Y., P. Doumalin, J. C. Dupré, and A. Germaneau: Strain, 2012, vol. 48(5), pp. 357-365. doi:10.1111/j.1475-1305.2011.00831.x
[26] P. Reu: Exp. Techn., 2014, vol. 38(5), pp. 1-3. doi:10.1111/ext.12111
[27] V. Doquet and B. Barkia: Mech. Mat., 2016, vol. 103, pp. 18-27.
[28] Y.L. Dong and B. Pan: Exp. Mech. 2017, vol. 57(8), pp. 1161-1181. doi:10.1007/s11340-017-0283-1.
[29] M. Grédiac, B. Blaysat and F. Sur: Exp. Mech., 2020, vol. 60(4), pp .509-534. DOI:10.1007/s11340-019-00579-z
[30] X. Hu, Z. Xie and F. Liu: Measurement, 2021, vol. 173, 108618. https://doi.org/10.1016/j.measurement.2020.108618
[31] A. Soula, D. Locq, D. Boivin, Y. Renollet, P. Caron and Y. Bréchet: J. Mater. Sci., 2010, vol. 45, pp. 5649-5659. DOI: 10.1007/s10853-010-4630-1
[32] G. Martin, C.W. Sinclair and J.-H. Schmitt: Scripta Mat., 2013, vol. 68(9), pp. 695-698. https://doi.org/10.1016/j.scriptamat.2013.01.017
[33] G. Martin, D. Caldemaison, M. Bornert, C. Pinna, Y. Bréchet, M. Véron, J.D. Mithieux and T. Pardoen: Exp. Mech. 2013, vol. 53(2), pp. 205-215. DOI:10.1007/s11340-012-9628-y
[34] K. Thibault, D. Locq, P. Caron, D. Boivin, Y. Renollet, Y. and Y. Bréchet : Mat. Sci. Eng. A, 2013, vol. 588, pp.14-21.
[35] T. Dessolier, P. Lhuissier, F. Roussel-Dherbey, F. Charlot, C. Josserond, J-J. Blandin and G. Martin: Mat. Sci. Eng. A., 2020, vol. 775. 138957. https://doi.org/10.1016/j.msea.2020.138957

Mis en forme : Anglais (États-Unis)
Code de champ modifié
Mis en forme : Anglais (États-Unis)
Mis en forme : Couleur de police : Automatique, Anglais (États-Unis)
Mis en forme : Couleur de police : Automatique
Mis en forme : Français (France)

[36] Kammers, A.D. and S. Daly: Exp. Mech. 2013, 53(9), 1743–1761. DOI:10.1007/s11340-013-9782-x
[37] Weidner, A. and H. Biermann: Adv. Eng. Mat., 2021, 23(4) 2001409
https://doi.org/10.1002/adem.202001409
[38] M. Kawasaki. and T.G. Langdon: J. Mater. Sci., 2007, vol. 42, pp. 1782-1796.
[39] F. Ashby: Acta Metall., 1972, vol. 20, pp. 887-897.
[40] F. Ashby: Adv. Appl. Mech., 1982, vol. 23, pp. 117-177.
[41] H.J. Frost and M.F. Ashby: Deformation Mechanism. Maps: The Plasticity and Creep of Metals and Ceramics, Pergamon Press, Oxford, New York, 1982, 166 pp.
[42] J. Weertman: J. Appl. Phys., 1957, vol. 28, pp. 1185-1189.
[43] J. Weertman: J. Appl. Phys., 1957, vol. 28, pp. 362.
[44] H. Lüthy, R.A. White, and O.D. Sherby: Mat. Sci. Eng., 1979, vol. 39, pp. 211-16.
[45] B. Fazan, O.D. Sherby, and J.E. Dorn: J. Met., 1954, vol. 6, pp. 919-922.
[46] N. Combe, F. Mompiou, and M. Legros: Phys. Rev. Mater., 2019, vol. 3, pp. 060601.
[47] H.P. Karnathaler: Phil. Mag. A, vol. 38(2), 1978, pp. 141-156.
https://doi.org/10.1080/01418617808239225
[48] M. Carrard and J.L. Martin: Phil Mag A, 1987, vol. 56(3), pp. 391-405.
[49] D. Caillard and J.L. Martin: Int. J. Mat. Res., 2009, vol. 100(10). pp. 1403-1410. DOI:10.3139/146.110190
[50] R. Le Hazif and J.-P. Poirier: Acta Metall., 1975, vol. 23, pp. 865-871.
[51] B. Bacroix, and J.J. Jonas: Textures Microstruct., 1987, vol. 8/9, pp. 267-311.
[52] A. Couret and D. Caillard: Acta Metall., 1988, vol. 36, pp. 2515-2524.
[53] D. Caillard and J.L. Martin: J. Phys., 1989, vol. 50, pp. 2455-2473.
[54] A. Albou, A. Borbely, C. Maurice and J.H. Driver: Phil. Mag., 2011, vol. 91, pp. 3981-4000.
[55] M. Arzaghi, B. Beausir, and L.S. Tóth: Acta Mater., 2009, vol. 57(8), pp. 2440-2453.
https://doi.org/10.1016/j.actamat.2009.01.041
[56] F.D. Rosi and C.H. Mathewson: JOM, 1950, vol. 2, pp. 1159-1167. https://doi.org/10.1007/BF03399117
[57] D. Picard, A. Dimanov, and J.L. Raphanel: Mat. Sci. Eng. A., 2018, vol. 732, pp. 284-297.
[58] M.F. Ashby and R.A. Verall: Acta Metall., 1973, vol. 21, pp. 149-63.
[59] R. Raj and M.F. Ashby: Metall. Trans., 1971, vol. 2, pp. 1113–1127.
[60] A. Dimanov, G. Dresen, E. Rybacki, and R. Wirth: J. Struct. Geol., 2007, vol. 29, pp. 1049-69.
[61] C.N. Ahlquist and R.A. Menezes: Mater. Sci. Eng., 1971, vol. 7, pp. 223-224.
[62] T.G. Langdon: Phil. Mag., 1971, vol. 21, pp. 689-700.
[63] M. Hillert and Gary R. Purdy: Acta Metall., 1978, vol. 26(2), pp. 333-340,
https://doi.org/10.1016/0001-6160(78)90132-3

Mis en forme : Couleur de police : Automatique, Anglais (États-Unis)

Mis en forme : Couleur de police : Automatique

Mis en forme : Couleur de police : Automatique

Mis en forme : Couleur de police : Automatique

Mis en forme : Couleur de police : Automatique

Mis en forme : Couleur de police : Automatique

Mis en forme : Police :(Par défaut) Times New Roman, 11 pt, Anglais (États-Unis)

Mis en forme : Police :(Par défaut) Times New Roman, 11 pt

[64] M. Hillert: Scr Metall., 1983, vol. 17(2), pp. 237-240, https://doi.org/10.1016/0036-9748(83)90105-9
[65] R.W. Balluffi and J.W. Cahn: Acta Metall, 1981, vol. 29(3), pp. 493-500, https://doi.org/10.1016/0001-6160(81)90073-0
[66] D.L. Beke, Yu. Kaganovskii and G.L. Katona: Progress Mat. Sci., 2018, vol. 98, pp. 625-674.
[67] O. Renk, A. Hohenwarter, S. Wurster, and R. Pippan: Acta Mater., 2014, vol. 77(100), pp. 401-410, doi: 10.1016/j.actamat.2014.06.010J.
[68] J.E. Harris: Nature 200, 1963, p1197. https://doi.org/10.1038/2001197a0
[69] P. Duval and O. Castelnau: J. Phys. IV, 1995, vol. 05 (C3), pp. 197-205.
[70] M. Montagnat and P. Duval: Earth. Planet. Sci Lett., 2000, Vol., 183(1-2), pp. 179-186, DOI:10.1016/S0012-821X(00)00262-4
[71] M. Tonks, P. Millett, W. Cai and D. Wolf: Scripta Mat., 2019, vol. 63(11), pp. 1049-1052, https://doi.org/10.1016/j.scriptamat.2010.07.034
[72] S.B. Lee, J. Jung and H.N. Han: Materials, 2020 vol. 13(2), 360, https://doi.org/10.3390/ma13020360
[73] A. Lens, C. Maurice and J.H. Driver: Mat. Sci. Eng. A, 2005, vol. 403(1-2) pp. 144-153, https://doi.org/10.1016/j.msea.2005.05.010
[74] M.L. Taheri, D. Molodov, G. Gottstein and A.D. Rollett: Z. Metall., 2005, vol. 96, pp.1166-1170, DOI: 10.3139/146.101157
[75] A. Rajabzadeh, F. Mompiou, S. Lartigue-Korinek, N. Combe, M. Legros, M., and D.A. Molodov: Acta Mater., 2014, vol. 77, pp. 223-235.
[76] N. Combe, F. Mompiou, M. Legros: Phys. Rev. B: Condens. Matter and Mater. Phys., 2016, vol. 93, pp. 024109.
[77] N. Combe, F. Mompiou, and M. Legros: Phys. Rev. Mater., 2019, vol. 3, pp. 060601.
[78] M. Larranaga, F. Mompiou, M. Legros, and N. Combe: Phys. Rev. Mater., 2020, vol. 4, pp.123606.
[79] N. Vigano, A. Tanguy, S. Hallais, A. Dimanov, M. Bornert, K.J. Batenburg, and W. Ludwig: Sci. Rep., 2016, vol. 6, pp.1-9.
[80] Y. Palizdar, D. San Martin, M. Ward, R.C. Cochrane, R. Brydson, and A.J. Scott: Mater. Charact., 2013, vol. 84, pp. 28-33.
[81] M. Verma, R. Mukherjee:. J. Appl. Phys., 2021, vol. 130, pp. 025305.
[82] G. Daveau : Thèse Ecole Centrale, Paris, 2012, https://tel.archives-ouvertes.fr/tel-00740650.

Mis en forme : Français (France)
Mis en forme : Français (France)
Code de champ modifié
Mis en forme : Français (France)
Mis en forme : Barré